

Lehigh University Lehigh Preserve

Theses and Dissertations

2012

Numerical simulation of nanoparticle delivery in microcirculation

Jifu Tan

Lehigh University

Follow this and additional works at: <http://preserve.lehigh.edu/etd>

Recommended Citation

Tan, Jifu, "Numerical simulation of nanoparticle delivery in microcirculation" (2012). *Theses and Dissertations*. Paper 1272.

This Thesis is brought to you for free and open access by Lehigh Preserve. It has been accepted for inclusion in Theses and Dissertations by an authorized administrator of Lehigh Preserve. For more information, please contact preserve@lehigh.edu.

Numerical simulation of nanoparticle delivery in microcirculation

by Jifu Tan

A Thesis

Presented to the Graduate and Research Committee

of Lehigh University

in Candidacy for the Degree of

Master of Science

in

Department of Mechanical Engineering and Mechanics

Lehigh University

May-2012

© 2012 Copyright
Jifu Tan

Thesis is accepted and approved in partial fulfillment of the requirements for the Master of Science in Department of Mechanical Engineering and Mechanics.

Numerical simulation of nanoparticle delivery in microcirculation

Jifu Tan

Date Approved

Thesis Director

(Name of Co-Director)

(Name of Department Chair)

ACKNOWLEDGMENTS

This thesis is the summary of the research work I did for the past 3 years. First, I want to thank my adviser Dr. Yaling Liu for the continuous support of my M.S. study and research. His mentoring in research, his hands-on training in programming, and his patience and motivation helped me a lot in writing the thesis. Without his guidance and support the thesis would not have been possible.

I would like to thank all the professors who lead me to study fluid mechanics, solid mechanics and how to numerically solve engineering problems. I am also grateful to Dr. Li Tao for his training on microfluidic fabrication. Many thanks to my lab mates including but not limited to Antony Thomas, Abhijit Ramchandran, Samar Shah, Manohara Mariyappa, and Qingjiang Guo. It is joyful to work with you.

In addition, I am in debt to my parents for supporting me studying over the last 20 years. I also appreciate my girlfriend's encouraging to the thesis writing. I love you all.

TABLE OF CONTENTS

LIST OF FIGURES	VII
LIST OF TABLES	IX
ABSTRACT.....	1
CHAPTER 1. INTRODUCTION	3
1.1 NANOPARTICLE BASED DRUG DELIVERY	3
1.2 PROPERTIES OF ENGINEERED NANOPARTICLES	4
1.3 MOTIVATIONS TO MODEL NANOPARTICLE TRANSPORT	5
CHAPTER 2. NUMERICAL METHODS FOR NANOPARTICLE DELIVERY IN BLOOD FLOW.....	8
2.1 NANOPARTICLE BROWNIAN DYNAMICS	8
2.2 RECEPTOR-LIGAND BINDING MODEL.....	9
2.3 RED BLOOD CELL AND FLUID-STRUCTURE INTERACTION MODEL	11
CHAPTER 3. INFLUENCE OF RED BLOOD CELLS ON NANOPARTICLE BINDING AND DISTRIBUTION IN MICROCIRCULATION	14
3.1 PARTICLE-PARTICLE AND PARTICLE-CELL INTERACTION MODEL.....	14
3.2 NANOPARTICLE DISPERSION COEFFICIENT CALCULATION.....	17
3.3 SIMULATION RESULTS	18
3.3.1 <i>Verification of NP diffusion coefficient with Taylor-Aris theory</i>	21
3.3.2 <i>The influence of shear rate on nanoparticle delivery</i>	22
3.3.3 <i>The influence of RBCs on NP binding</i>	27
3.4 MICROFLUIDIC EXPERIMENTAL VALIDATION	31

CHAPTER 4. NANOPARTICLE DISTRIBUTION IN A VASCULAR NETWORK	33
4.1 SHAPE DEPENDENT NANOPARTICLE BINDING DYNAMICS.....	34
4.2 DISTRIBUTION OF NANOPARTICLES OF DIFFERENT SIZES	36
4.3 DISTRIBUTION OF NANOPARTICLES OF DIFFERENT SHAPES AND SIZE UNDER VARIOUS SHEAR RATES ..	37
4.4 INFLUENCE OF PÉCLET NUMBER ON NANOPARTICLE DISTRIBUTION PATTERN	44
CHAPTER 5. CONCLUSION AND FUTURE WORK.....	46
REFERENCE.....	50
VITA.....	56

LIST OF FIGURES

Figure 1. (A) Geometry and mesh of RBC; (B) Mesh of RBC and fluid.....	11
Figure 2. (A) 3D simulation of nanoparticle-RBC interaction; (B) Cross-section view of nanoparticle-RBC interaction.	14
Figure 3. Illustration of the two time steps and mapping algorithms used in the simulation. (A) Overlapping happens when the same time step dt is used for both RBCs and NPs. (B) different time steps are used for RBCs (dt) and NPs (dt_t) so that the overlapping is avoided. (C) Illustration of linear interpolation for RBC's intermediate positions.	16
Figure 4. Illustration of three different simulation setups: (A) pure particles; (B) same NP dosage mixed with RBCs; (C) same effective particle concentration mixed with RBC s.	20
Figure 5. (A) Taylor-Aris effect for the NP diffusion in vessel. (B) Overall Mean square displacement (MSD) for NPs in flow direction, which is a quadratic function of time t ; (C) Instantaneous Mean Square Displacement (IMSD) for NPs in flow direction, the average instantaneous diffusion coefficient is about $2.2 \times 10^{-8} \text{ cm}^2/\text{s}$ (here $dt_t=0.01\text{s}$, which is different from NP-RBC simulation case).	21
Figure 6. Simulation of RBCs and NPs interaction under a shear flow. (A) initial configuration of the model; (B) a snap shot of the model at 0.74 s.	23
Figure 7. Nanoparticle distribution profile across the vessel. (A) initial NP distribution profile with RBCs; (B) NP distribution profile with RBCs at 1 s; (C) initial NP distribution profile without RBCs; (D) NP distribution profile without RBCs at 1 s.	24
Figure 8. The overall mean square displacements (MSD) of the particles with RBCs and without RBCs under a shear rate of 8 s^{-1} , which show that RBCs enhance the dispersion for both larger NPs and smaller NPs, but in slightly different ways. (A) NPs with size of 100 nm; (B) NPs with size of 10 nm, the zoom-in subplot show smaller NPs are trapped initially by RBCs. Instantaneous mean square displacement (IMSD) of the particles with RBCs and without RBCs under shear rate of 8 s^{-1} : (C) NPs with size of 100 nm; (D) NPs with size of 10 nm.	26
Figure 9. Mean square displacement of NPs under shear rates of 8 s^{-1} and 16 s^{-1} with RBCs and without RBCs. (A) 100 nm size of NPs; (B) 10 nm size of NPs.	27
Figure 10. Particle distribution profile at time $t=7.5\text{s}$. (A) NPs with RBCs case; (B) NPs without RBCs.	28
Figure 11. (A) Nanoparticle binding time histories with and without RBCs of the same effective nanoparticle density; (B) Nanoparticle binding time histories with and without RBCs of the same NP dosage.	29
Figure 12. NPs binding rates with RBCs and without RBCs under same density and same dosage. Such increased binding rate is explained by the higher NP concentration in the cell-free-layer and larger dispersion rate.	30

Figure 13. Fluorescence intensity across the channel in microfluidic tests, the error bar is plotted based on 10 runs of tests: (A) with RBCs; (C) without RBCs; (B) and (D): simulated NP distribution across the channel in the simulation with and without RBCs from Figure 10.....	32
Figure 14. A bifurcation microchannel for NP deposition simulation. (A) geometry dimensions; (B) illustration of straight section and bifurcation area.....	34
Figure 15. Trajectory snapshots of a nanosphere (A) and a nanorod (B) under shear flow. The arrows illustrate the adhesive force once the particles interact with the wall. ..	34
Figure 16. Normalized binding probability for (A) NP size of 100 nm; (B) NP size of 200 nm.	36
Figure 17. Distribution of nanospheres of different sizes. Half of the channel is shown in the figure due to symmetry. Top: 100 nm; Bottom: 200 nm.	37
Figure 18. A snap shot of the particle distribution in the branched vessel for (A) spheres; (B)rods.	38
Figure 19. 100 nm nanoparticle distribution along the channel .(A)50 $\mu\text{m/s}$, (B)100 $\mu\text{m/s}$, (C) 200 $\mu\text{m/s}$, (D) 300 $\mu\text{m/s}$, (E) 500 $\mu\text{m/s}$	41
Figure 20. Adhesion of NPs depends on particle shape and their orientation. Nanorods have smaller contact area and bonding force during transient rotation, but maximal bonding force after laying down with long axis aligned with wall	42
Figure 21. 200 nm Nanoparticle distribution along the channel .(A)50 $\mu\text{m/s}$, (B)100 $\mu\text{m/s}$, (C) 200 $\mu\text{m/s}$, (D) 300 $\mu\text{m/s}$, (E) 500 $\mu\text{m/s}$	43
Figure 22. Ratio of the number of deposited NPs on branched region and straight section depends on the Péclet number. The simulation data are fitted by quadratic lines through least square method. (A) 100 nm NPs; (B) 200 nm NPs.....	45

LIST OF TABLES

Table 1. Parameters used in the receptor ligand binding model	10
Table 2. Parameters used in Lennard-Jones potential and Morse potential.....	15

Abstract

Multifunctional nanomedicine holds considerable promise as the next generation of medicine that allows for targeted therapy with minimal toxicity. To evaluate the delivery efficiency of Nanoparticles (NPs), it is important to study their transport, binding and distribution in blood flow. For blood flow in capillaries, arterioles and venules, the particulate nature of the blood and physiological conditions needs to be considered in the delivery process. The existence of the cell-free-layer, NP-cell interaction, particle shape and vessel geometry will largely influence the dispersion, binding rates and distribution, thus impact targeted delivery efficacy. In this thesis, a particle-cell hybrid model is developed to model NP transport, dispersion, and binding dynamics in blood suspension. The motion and deformation of red blood cells is captured through the Immersed Finite Element Method. The motion and adhesion of individual NPs are tracked through Brownian adhesion dynamics. The influence of red blood cells, vascular flow rate, particle size, shape and vessel geometry effect on NP distribution and delivery efficacy is characterized. With red blood cells, a non-uniform NP distribution profile with higher particle concentration near the vessel wall is observed, which leads to over 50% higher particle binding rate compared to the case without red blood cell. The tumbling motion of red blood cells in the core region of the capillary is found to enhance NP dispersion, and dispersion rate increases with shear rate. The simulation results also indicate that NPs with smaller size and rod shape have higher binding rates. The binding dynamics of rod-shaped NPs is found to be dependent on their initial contact points and orientations to the

wall. Moreover, it is found that Péclet number plays an important role in determining the fraction of NPs deposited in the branched region and the straight section. Simulation results also indicate that NP binding rate decreases with increased shear rate. Dynamic NP re-distribution from low to high shear rates is observed due to the non-uniform shear stress distribution over the branched channel. Results from this study contribute to the fundamental understanding and knowledge on how the particulate nature of blood, size, shape and vessel geometry influences NP delivery and distribution, which will provide mechanistic insights on the nanomedicine design for targeted drug delivery applications.

Chapter 1. Introduction

1.1 Nanoparticle based drug delivery

Over the past decades, various nanoplatforms, including liposomes[1-2], polymeric micelles[3-6], quantum dots[7-8], Au/Si/polymer shells[9-11], dendrimers[12-14], and Nanoparticles[15] have been emerged and developed as smart drug carriers and image probing agents. Many unique properties and potential applications offered by NPs attract the attentions of scientist, engineers and medical researchers. For example, NPs can imbibe drug into their core or coat drug to their surface to fight against cardiovascular disease. Their half time in circulation and selectively distribution can be modulated by their size and shape which can be achieved easily with advanced microfabrication technology. Active and controlled drug release can be triggered by the properties of the surrounding environment, such as PH level, light intensity, and temperature. Iron oxide NPs can be functionalized with different ligands to target the particular receptors expressed on cancer cells. The magnetic properties of the Iron oxide enhance the image in magnetic resonance imaging[16-17]. Gold nanocages with large absorption cross section per volume can convert light into heat for photothermal destruction under the excitation of laser[18]. The research work in this thesis is focused on modeling NP transport, binding and distribution under the influence of red blood cells and complex vessel geometries.

1.2 Properties of engineered nanoparticles

Properties such as size, shape, surface chemistry play an important role in NP binding and distribution. As a key characteristic of NP, size has been studied extensively in literature. For example, it is known that spherical particles bigger than 200 nm are efficiently filtered by liver, spleen and bone marrow, while particles smaller than 10 nm can be quickly cleared by kidney or through extravasation, thus making 10-200 nm as an ideal size range for the circulating spherical carriers. Similar to size, shape is also a fundamental property of micro/nanoparticles that is critical for their intended biological functions. Most nanoparticles have spherical shape due to surface tension. With the advanced nanofabrication techniques, different shapes and forms of NP have emerged in recent years with unique geometrical, physical and chemical properties. For example, nanorods with suitable aspect ratio have been fabricated as a novel contrast agent for both molecular imaging and photothermal cancer therapy[19]; asymmetrically functionalized AuNPs have been assembled to build nanochains[20]; superparamagnetic iron oxide based nanoworms are studied for tumor targeting[21], and nanonecklaces are assembled using gold nanoparticles by covalent bonding[22]. It has been reported that cylindrically shaped filamicelles can effectively evade non-specific uptake by the Reticulo-Endothelial System, allowing persistent circulation for up to one week after intravenous injection[23]. Besides size and shape, surface functionalization of nanoparticle determines the adhesion capability of NPs. For nanorods, it is reported that Janus coating at the two ends of nanorods leads to better adhesion compared to uniform coating[24-25]. Protein adsorption and phagocytosis of particles *in vivo* has been shown to be reduced by the

immobilization of polyethylene glycol (PEG) on them[26]. Many studies apply PEG based copolymer modification which enhances circulating half-life while contributing to decreased uptake in nontargeted cells. On the other hand, phage display based targeting on various organs has been performed by the immobilization of peptides on them. Selective localization of bacteriophage to brain and kidney blood vessels were performed by applying peptides capable of targeting and showed up to 13-fold selectivity for these organs[27].

1.3 Motivations to model nanoparticle transport

Although NPs offer many advantages over conventional drug carriers, their transport, binding and distribution are not fully understood. First, NPs are too small to be visualized *in vivo* with dimensions between ten to a few hundred nanometers; it is challenging to track NP trajectories *in vivo*. Second, biological environment *in vivo* for NP is very complex, which involves blood flow, circulation, elimination and extravasation. NPs cannot always reach targeted site because they may be filtered by liver, eliminated by spleen, bonded to healthy cells.

To achieve better delivery efficacy, the diseased region type, size, location, and the patient's physical parameters (e.g. vascular diameter, blood flow rate, surface area, blood components) need to be considered. The NP targeted delivery in vascular system involves interplay of transport, hydrodynamic force, and multivalent interactions with targeted biosurfaces. It is very challenging to explore these phenomena experimentally *in vivo*, due to the small size of NPs, the dynamic delivery process, and the complex vascular environment. Thus a mathematical tool that can predict and evaluate the NP

binding and distribution is necessary. At microscale, current theoretical works of NP deposition are limited to simple spherical particles under an ideal condition in a 2D channel under shear flow[28-30], which cannot predict the behaviors of particles of various designs in blood flow under complex vascular conditions. At macroscale, continuum convection-diffusion-reaction models have been widely used in modeling drug delivery process. For example, Shipley *et al.*[31] and Modok *et al.*[32] modeled delivery of spherical NPs in tumor. Mahmoudi *et al.*[33] and Li *et al.*[34] performed computational fluid dynamics studies of magnetic NPs in vascular flow. Liu *et al.*[35] and Zhang *et al.*[36] studied the deposition of NPs in lung airway. However, continuum model cannot provide details such size, shape, ligand-receptor density, and shear dependent effect on NP binding.

Another concern is that little is known about NP binding and distribution under the influence of red blood cells (RBCs) and in different vascular geometries. When blood flows through vessels, the two-phase nature of the blood becomes important as the diameter of RBCs becomes comparable to the vessel diameter. Various unique phenomena have been observed in microcirculation due to the particulate nature of the blood, such as (a) vessel diameter dependent apparent viscosity: Fåhræus–Lindqvist effect; (b) existence of a cell-depleted layer near the wall: cell free layer; and (c) blunt velocity profile. These phenomena have significant impact on NP targeted delivery efficiency. First, targeted binding to diseased cells requires NPs to move close to the vascular wall, i.e, in a near wall binding-layer. Such a near wall binding-layer is coincident with the cell-free layer, with the addition of NPs in such layer. However, the thickness of such cell-free layer varies with vascular conditions, thus changes the binding

properties. Second, the existence of blood cells in the core region of blood streams changes the NP dispersion rate through cell-NP interaction. Many blood vessels consist the whole vascular network. It is reported experimentally NPs have different binding preference in microvascular network[37], i.e., more particles bonded to the bifurcation region than the straight section of the channel. With these in mind, it is natural to ask: What is the effect of RBCs on NP delivery? Is NP binding vessel geometry dependent? What controls NP distribution pattern in branched vessels? Thus, it is crucial to characterize NP transport with RBCs and under different vascular flow conditions through a mathematical model[38].

This thesis attempts to answer these questions through numerical simulations. A combined continuum fluid model and Brownian adhesion dynamics model is developed to simulate NP transport in blood flow. The thesis is organized as follows. Chapter 1 introduces the background of NP delivery and the motivation of this study. Chapter 2 discusses the methods used to simulate particle motion and fluid flow. Chapter 3 gives detailed simulation process and results of the NP delivery with RBCs considered. Chapter 4 presents NP distribution in a simplified branched vessel. Lastly, the future work is described in Chapter 5.

Chapter 2. Numerical Methods for Nanoparticle Delivery in

Blood Flow

In this chapter, techniques used to model NP transport and diffusion will be introduced first. The model of red blood cells and finite element based computational fluid methods are described next. Finally, the interaction potentials between NPs, NP-RBCs are presented.

2.1 Nanoparticle Brownian dynamics

Brownian motion theory points out that small particles immersed in fluids are subjected to the random collisions from the surrounding liquid molecules[39-41]. Patankar *et al.*[42] proposed an algorithm for direct numerical simulation of Brownian motion by adding random disturbance in fluids. At microscale, the Brownian motion is negligible compared to larger drag forces (> 50 pN for particle size > 1 μm)[43]. At nanoscale, Brownian force outweighs the drag force, becoming a dominant force to drive NP near vessel wall. The random forces $\mathbf{R}(t)$ and random Torques $\mathbf{T}(t)$ acting on a NP are responsible for Brownian motion and satisfy the fluctuation-dissipation theorem[44]:

$$\langle \mathbf{R}_i(t) \rangle = 0, \quad \langle \mathbf{T}_i(t) \rangle = 0, \quad (1)$$

$$\langle \mathbf{R}_i(t) \mathbf{R}_j(t') \rangle = 2 k_B T \beta_i \delta_{ij} \delta(t-t') \boldsymbol{\delta} \quad (2)$$

$$\langle \mathbf{T}_i(t) \mathbf{T}_j(t') \rangle = 2 k_B T \beta_r \delta_{ij} \delta(t-t') \boldsymbol{\delta}^{\prime} \quad (3)$$

where, δ is the unit-second order tensor, δ_{ij} is the Kronecker delta, $\delta(t - t')$ is the Dirac delta function, $k_B T$ is thermal energy of system, β_t and β_r are translational and rotation friction coefficient, respectively.

The friction coefficient depends on several physical parameters, such as fluid viscosity, size and shape of the NP. The friction coefficient for particles can be easily derived from Stokes' law:

$$\beta_t = 3\pi\mu d \quad (4)$$

$$\beta_r = \pi\mu d^3 \quad (5)$$

where μ is the fluid viscosity, d is the diameter of particle. The velocity of a particle moving under a deterministic force in a fluid with velocity \mathbf{V}_f is given by:

$$\mathbf{V}_p = \left(\frac{\mathbf{F}_{\text{det}}}{\beta_t} + \mathbf{V}_f \right) + \left(\frac{\mathbf{T}_{\text{det}}}{\beta_r} + \boldsymbol{\omega}_f \right) \times \mathbf{r} \quad (6)$$

where \mathbf{V}_f and $\boldsymbol{\omega}_f$ are fluid translational and angular velocity vectors, respectively; \mathbf{V}_p is the particle velocity; \mathbf{r} is the position vector from the centroid of NPs; \mathbf{F}_{det} and \mathbf{T}_{det} are the total deterministic force and torque acting on the NP (including Brownian force/torque, adhesion force/torque, etc.).

2.2 Receptor-ligand binding model

Receptor and ligand binding process has been studied extensively. Bell established the theoretical framework for cell adhesion mediated by reversible bonds[45-46]. Ward also listed some 'best' values for parameters related to the cell-substrate adhesion[47]. Motivated by their work, the receptor-ligand binding process is governed by equation:

$$\frac{\partial N_b}{\partial t} = k_f(N_l - N_b)(N_r - N_b) - k_r N_b \quad (7)$$

where N_b is the number of formed receptor-ligand pairs; k_f is the forward binding rate, N_l is the ligand density on the particle surface; N_r is the receptors on the vessel wall; k_r is bond reverse binding rate.

The parameters used in our model are chosen according to physiological values reported in literature and are summarized in Table 1 :

Table 1. Parameters used in the receptor ligand binding model

Parameters	Value	reference
Ligand density N_l	$200/\mu\text{m}^2$	[47]
Receptor density N_r	$100/\mu\text{m}^2$	[47]
Unstressed bond length L	20 nm	[45-46]
Bond spring constant	0.5 dyn/cm	[47]
Forward binding rate k_f	$1 \times 10^6 \text{ nm}^2/\text{s}$	[48]
Reverse binding rate k_r	$1 \times 10^{-2} / \text{s}$	[48]

According to these parameters, the binding force for a single ligand-receptor bond is around 5 pN which is within the range of Bell's estimation 40 pN[45]. In the model, as long as adhesive force induced by the total bonds is larger than drag force, the particle is assumed to be bonded to the wall.

2.3 Red Blood Cell and Fluid-Structure Interaction Model

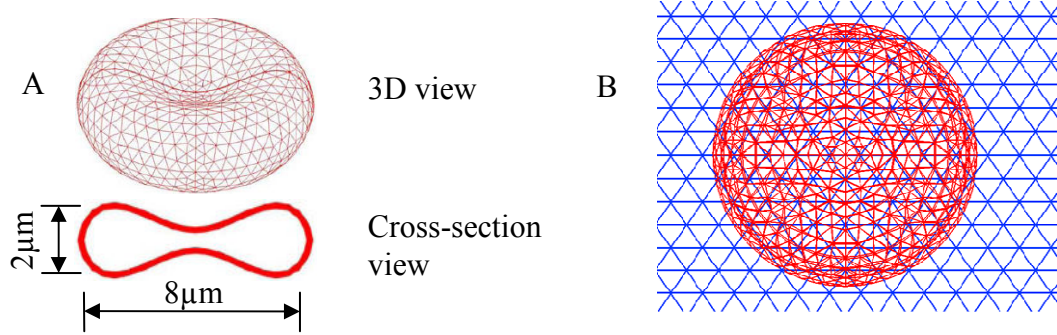


Figure 1. (A) Geometry and mesh of RBC; (B) Mesh of RBC and fluid

In the simulation, RBCs are modeled as flexible thin membranes enclosing a fluid [49-50], as shown in Figure 1. Both the cytoplasm inside the RBC and the blood plasma outside the RBC have a viscosity of around 0.01 dyn·s/cm, thus are treated as the same fluid. A Mooney–Rivlin strain energy function similar to that of our previous work[49-50] and others[51-53], is used to depict the material behavior of the RBC membrane:

$$W = C_1 (I_1 - 3) + C_2 (I_2 - 3) \quad (8)$$

with the material properties specified by constants C_1 and C_2 . I_1 and I_2 are the functions of the invariants of the Cauchy-Green deformation tensor \mathbf{C} .

RBCs and their interaction with fluid flow are modeled by the IFEM formulation[49-50]. The IFEM was developed by Zhang *et al.* and Liu *et al.*[54-57] to solve coupled fluid-structure interaction problems. Because much of the method has been derived in detail in works[54-57], we will just briefly list out the IFEM procedures below, and refer the interested reader to those for further details. The fluid in the

simulation is assumed to be an incompressible viscous fluid governed by the Navier–Stokes equations:

$$\rho \left(\frac{\partial \mathbf{v}_f}{\partial t} + \mathbf{v}_f \cdot \nabla \mathbf{v}_f \right) = -\nabla p + \mu \nabla^2 \mathbf{v}_f \quad (9)$$

$$\nabla \cdot \mathbf{v}_f = 0 \quad (10)$$

where \mathbf{v}_f is the fluid velocity in the fluid domain. Motivated by Peskin’s immersed boundary method[58-60], as in IFEM[57], an extra volumetric force is introduced to avoid the complex re-meshing usually encountered in the fluid-structure interaction problems. This extra force \mathbf{F}^{FSI} , called the fluid-structure interaction force, is defined as:

$$\mathbf{F}^{\text{FSI}} = \begin{cases} -(\rho^s - \rho^f)(\dot{\mathbf{v}}^s - \mathbf{g}) + \nabla \cdot (\boldsymbol{\sigma}^s - \boldsymbol{\sigma}^f), & \text{in } \Omega^s \\ 0, & \text{in } \Omega \setminus \Omega^s \end{cases} \quad (11)$$

where \mathbf{v} is the velocity, ρ is the density and $\boldsymbol{\sigma}$ is the Cauchy stress tensor. s and f denote for solid and fluid respectively.

For a Newtonian fluid of uniform viscosity, $\boldsymbol{\sigma}^f$ can be written as:

$$\boldsymbol{\sigma}^f = -p^f \mathbf{I} + \mu [\nabla \mathbf{v}^f + (\nabla \mathbf{v}^f)^T] \quad (12)$$

where μ is the fluid viscosity and p^f is the hydrostatic pressure.

To interpolate between the Eulerian and Lagrangian domains, a restriction operator L_t^s from Ω onto Ω^s is needed to make the system complete:

$$(L_{\Omega_t^s} \psi)(\mathbf{X}, t) \equiv \psi(\mathbf{x}(\mathbf{X}, t), t), \quad \forall \mathbf{X} \in \Omega_0^s \quad (13)$$

With this mapping function, we obtain the solid velocity and displacement from the Eulerian space as:

$$\mathbf{v}^s = L_t^s \mathbf{v}, \quad \text{in } \Omega^s \quad (14)$$

$$\frac{\partial \mathbf{u}^s}{\partial t} = \mathbf{v}^s, \quad \text{in } \Omega^s \quad (15)$$

Eqn.(14) basically interpolates the solid velocity from the fluid field through a mapping function.

The coupled fluid-structure interaction equations are solved through finite element method. The weak forms of the immersed system and other details can be found in previous publication[57] . To reduce numerical oscillations, the velocity test function is employed along with stabilization parameters. Using integration by parts and the divergence theorem, the Patrov-Galarkin weak form is obtained. Then, the nonlinear system is solved using the Newton-Raphson method. Moreover, Generalized Minimum Residual (GMRES) iterative algorithm is employed to improve computation efficiency and to compute residuals based on matrix-free techniques[61].

Chapter 3. Influence of Red Blood Cells on Nanoparticle binding and distribution in microcirculation

Blood is a complex biological fluid made of components such as red blood cells (RBC), monocytes, platelets, proteins, etc. RBCs occupy about 45% of the blood by volume. In this model, RBCs are considered to study their effect on NP transport, diffusion and binding. Various potentials are introduced to model particle-particle, and cell particle interactions. Different time steps are used to track NP and RBCs motion.

3.1 Particle-Particle and Particle-Cell Interaction Model

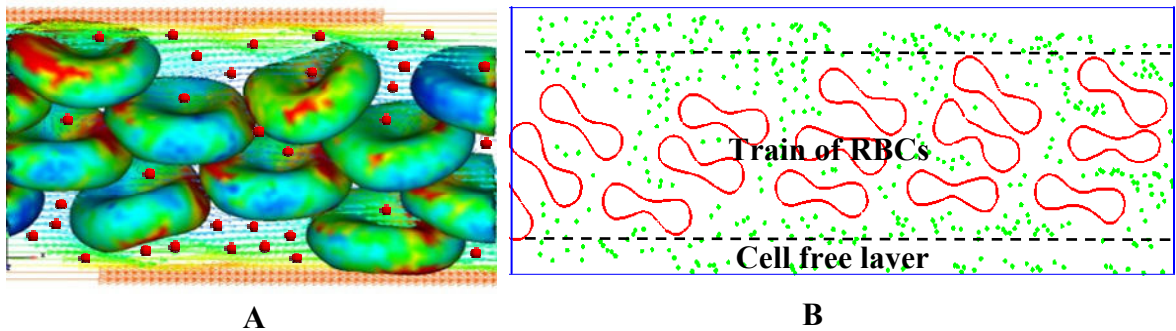


Figure 2. (A) 3D simulation of nanoparticle-RBC interaction; (B) Cross-section view of nanoparticle-RBC interaction.

A schematic illustration for Particle-cell interaction is given in Figure 2. The motion of NPs is governed by Brownian adhesion dynamics[7]. As described in Chapter 2, RBCs and their interaction with fluid flow is modeled by IFEM formulation[49-50].

For NPs, a Lennard-Jones potential is introduced to characterize the interaction between individual particles.

$$V(r) = 4\varepsilon\left[\left(\frac{\sigma}{r}\right)^{12} - \left(\frac{\sigma}{r}\right)^6\right] \quad (16)$$

$$F(r) = -\frac{dV(r)}{dr} = \frac{24\varepsilon}{\sigma}\left[2\left(\frac{\sigma}{r}\right)^{13} - \left(\frac{\sigma}{r}\right)^7\right] \quad (17)$$

where σ is the distance at which the energy is zero, ε is the strength of the potential energy.

A short-range repulsive Morse potential is used to avoid overlapping between NPs and RBCs:

$$\phi(r) = D_e[e^{2\beta(r_0-r)} - 2e^{\beta(r_0-r)}] \quad (18)$$

$$f(r) = -\frac{\partial\phi(r)}{\partial r} = 2D_e\beta[e^{2\beta(r_0-r)} - e^{\beta(r_0-r)}] \quad (19)$$

where r_0 and D_e stand for the zero force length and surface energy respectively, and β is a scaling factor. Similar cell-particle collision model has been used by Almomani *et al.* [62] to study the erythrocyte-platelet interaction in blood flow, where the collision forces were modeled as spring forces between the surfaces of the colliding particles and erythrocytes. The parameters used in the simulation model are listed in Table 2.

Table 2. Parameters used in Lennard-Jones potential and Morse potential

Parameter	ε	σ	D_e	β	r_0
Value	10^{-15} J	200.0 nm	4.1×10^{-13} J	$2 \mu\text{m}^{-1}$	0.5 μm

It should be noticed that different time steps are used to track particle motion and blood cell deformation, i.e., a smaller time step dtt for NPs and a larger time step dt for blood cell-fluid interaction, as shown in Figure 3A and 3B. The time steps are determined by the flow velocity and the particle diffusion speed. A small time step is needed to capture the high speed Brownian motion while a larger time step can be used for relatively slow RBC-fluid interaction. Similar different time steps had been used to capture the many-particle binding dynamics with a receptor coated surface by Arieh *et al.*[63].

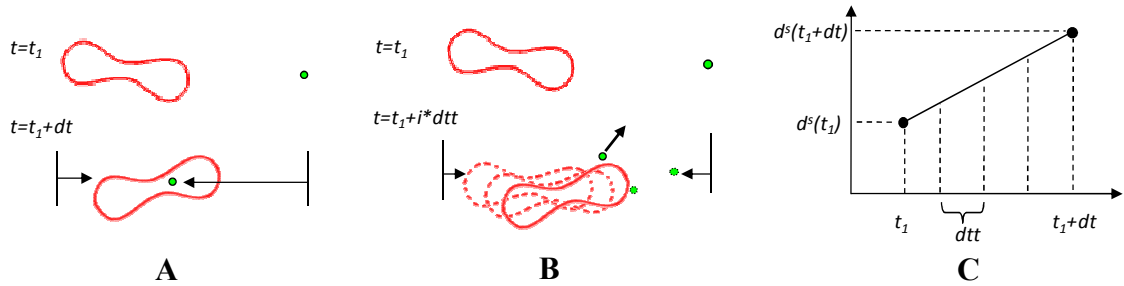


Figure 3. Illustration of the two time steps and mapping algorithms used in the simulation. (A) Overlapping happens when the same time step dt is used for both RBCs and NPs. (B) different time steps are used for RBCs (dt) and NPs (dtt) so that the overlapping is avoided. (C) Illustration of linear interpolation for RBC's intermediate positions.

However, a few problems may arise due to the using of varied time stepping. When NPs approach the RBCs, the shortest distance L_s between NPs and the RBCs' surface is calculated and compared with a cut-off distance R_{cut} defined for implementation of Morse potential. For $L_s < R_{cut}$, the Morse potential applies a repulsive force so that NPs can be repelled away. However, the particles may penetrate into the RBCs if the distance the RBCs travel per time dt is larger than R_{cut} which usually happens

unless a very small flow velocity is applied. To resolve this problem, the time step for RBCs dt is divided into a number of equally small time step dtt , as shown in Figure 3C, and the RBC position virtual images at intermediate time intervals are interpolated by:

$$d^s(t_1 + i * dtt) = d^s(t_1) + \frac{d^s(t_1 + dt) - d^s(t_1)}{dt} \times i \times dtt \quad (20)$$

Such virtual images for RBCs are established only for cell-particle repulsive force calculation. In the simulation, R_{cut} is 400 nm. If the fluid velocity is 40 $\mu\text{m/s}$, to avoid particle penetration, the maximum time step is chosen to be 0.01s. However, during 0.01s, NP travels 296 nm due to Brownian motion. Also due to the exponential form of Morse potential and power form of Lennard-Jones potential, if NP jumps with a big distance, the repulsive force generated by two potentials will repel NP out of the fluid domain. To be safe, dtt is chosen as 0.00001s to make sure NP travels about 9 nm each time step. In summary, the position of RBCs is updated based on larger time step dt while NPs positions are updated on smaller time step dtt . The collision between the RBCs and NPs are captured by RBC virtual images at intermediate steps. Such two time step algorithm will largely increase the simulation speed without losing accuracy.

3.2 Nanoparticle dispersion coefficient calculation

NP dispersion coefficient will be calculated under various flows conditions. The dispersion coefficient can be evaluated by tracking the motion of NPs and calculate the mean square displacements[64-66]. Since margination process is important in nanoparticle attachment to vascular wall and drug delivery, we focus on the particle dispersion in the radial direction. The mean square displacement (MSD) is defined as

$$\langle \xi(t, \tau) \rangle = \frac{1}{N_c} \sum_{i=1}^{N_c} \frac{1}{N} \sum_{\alpha=1}^N [r_i^\alpha(\tau+t) - r_i^\alpha(\tau)]^2 \quad (21)$$

where $r_i^\alpha(\tau+t)$ is the radial-coordinate of particle α from initial configuration i at time t starting from τ . N is the total number of particles, N_c is the total number of simulation runs. τ is chosen to be large enough so that there is no dependence on the initial particle distribution. Then the Overall Diffusion Coefficient (ODC) can be obtained by

$$D(t, \tau) = \frac{1}{2} \frac{d}{dt} \langle \xi(t, \tau) \rangle \quad (22)$$

It should be noted that NPs dispersion in blood vessel is not a free diffusion process because NPs have instantaneous collisions with the RBCs and vessel wall. In this sense, the mean square displacement defined before cannot truly reflect the distance NPs traveled at each time step. Thus to better reflect the interaction of RBCs on NP diffusion, Instantaneous Diffusion Coefficient (IDC) is defined as

$$\langle \xi(dtt) \rangle = \frac{1}{N_c} \sum_{i=1}^{N_c} \frac{1}{N} \sum_{\alpha=1}^N [r_i^\alpha(t+dtt) - r_i^\alpha(t)]^2 = 2D_I dtt \quad (23)$$

where dtt is the small time step, D_I is the Instantaneous Diffusion Coefficient, $\langle \xi(dtt) \rangle$ is the Instantaneous Mean Square Displacement (IMSD).

3.3 Simulation Results

Since RBCs consist of almost 50% of the blood and are dominant over all other blood cells, only RBCs and NPs are modeled in the simulation. The combined Immersed Finite Element and particle Brownian dynamics model is used to model the NPs delivery process in microcirculation.

The number of RBCs inside the simulation domain is determined by the volume ratio of RBC to blood to achieve a RBC concentration close to the hematocrit of human blood (normally in the range of 30-55% in larger arteries and drops to 10-15% in capillaries[67]). In our simulation, a number of RBCs are put into the fluid domain to reach a hematocrit of around 36%. NP size is chosen between 10~200 nm which is recommended in literature[68-70]. NP concentration is around 1 $\mu\text{g}/1\mu\text{L}$ which is consistent with cancer targeted PLGA-PEG-COOH NP suspension of 10 $\mu\text{g}/\mu\text{L}$ [71], Paclitaxel-loaded TPGS-emulsified PLGA NPs with concentration of 10 mg/mL [72] and Antitubercular drugs loaded PLG-NP with concentration of 25 $\text{mg}/2\text{mL}$ [73]. Period boundary conditions are applied to the left and right side of boundaries so that RBCs and NPs exit from one end of the channel can re-enter the inlet. Based on Einstein–Stokes equation, theoretical diffusion coefficient for the NPs with a diameter of 100 nm is 2.2×10^{-8} cm^2/s . The average flow rate in the channel is 20 $\mu\text{m}/\text{s}$, which is within physiological speed range from 10-100 $\mu\text{m}/\text{s}$ for capillary vessel with diameter between 10 and 20 μm [74].

In the simulations, two independent sets of meshes are used for RBCs and fluid domain. Each Red blood cell consists of 1534 nodes and 4340 elements. The fluid mesh has 5705 nodes and 16632 elements. A time step of 0.00001 s and 0.002 s are used for the NP Brownian dynamics and RBCs-fluid interaction simulations, respectively. To clearly illustrate both NPs and RBCs, cross-sectional views are used in the simulation snapshots throughout this thesis.

To explore the effect of RBCs on NP delivery, three sets of simulation setups are used: pure particles, particles mixed with RBCs to keep the total amount of particle same

as pure particle case, and particles mixed with RBC to keep the same effective concentration excluding RBC volume, as shown in Figure 4. The pure particle case is used as a control. The second case is used to check the influence of RBCs on particle dispersion and binding if the same dosage of NPs is considered. The third case is used to check the influence of RBCs on particle dispersion and binding if volume exclusion effect of the RBCs is removed, thus the effective particle concentration is the same as the pure particle case. Normally NP suspension will increase the effective viscosity of blood. In our work, NP volume concentration is about 0.08%, based on the results reported in Lee *et.al.*[75], under such a low concentration, the enhancement of NP on viscosity is less than 1%, thus it is reasonable to ignore the viscosity enhancing effect.

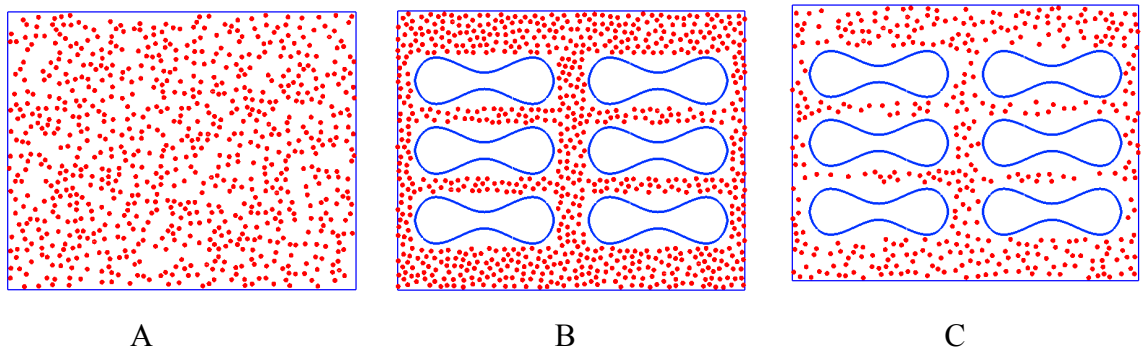


Figure 4. Illustration of three different simulation setups: (A) pure particles; (B) same NP dosage mixed with RBCs; (C) same effective particle concentration mixed with RBCs.

3.3.1 Verification of NP diffusion coefficient with Taylor-Aris theory

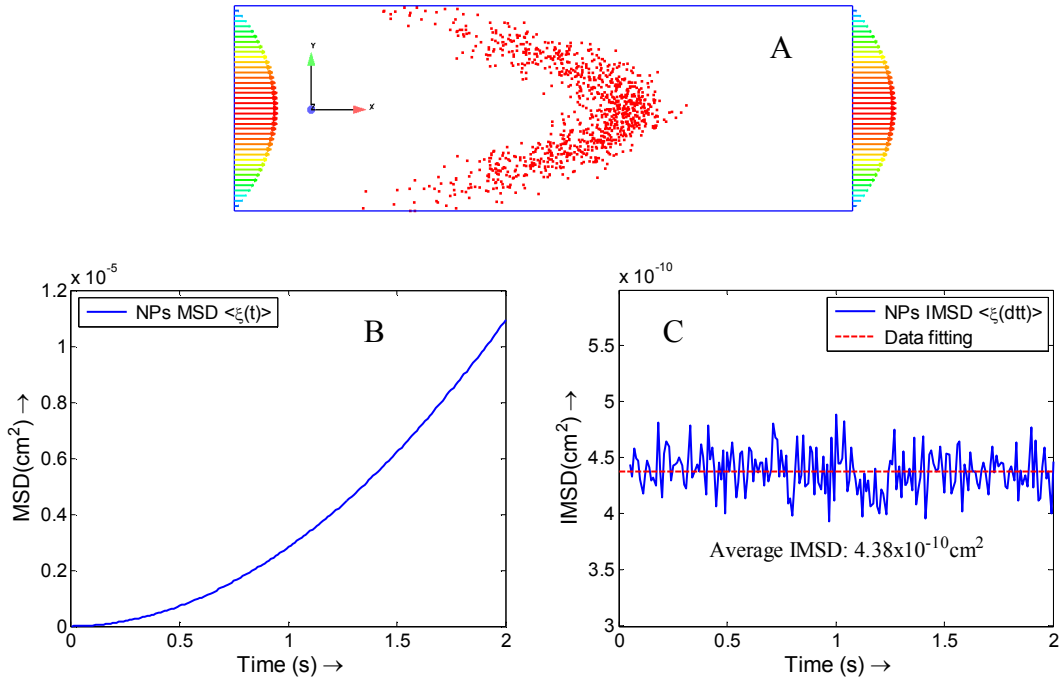


Figure 5. (A) Taylor-Aris effect for the NP diffusion in vessel. (B) Overall Mean square displacement (MSD) for NPs in flow direction, which is a quadratic function of time t ; (C) Instantaneous Mean Square Displacement (IMSD) for NPs in flow direction, the average instantaneous diffusion coefficient is about $2.2 \times 10^{-8} \text{ cm}^2/\text{s}$ (here $dt=0.01\text{s}$, which is different from NP-RBC simulation case).

When NPs are injected into the blood flow, they spread out across the vessel under the combined effects of diffusion and fluid flow. It is derived analytically that the particle concentration generated is centered on a point which moves with the mean speed of flow and is symmetrical about this point in spite of the asymmetry of the flow[76], as shown in Figure 5. The diffusion coefficient for NPs with a diameter of 100 nm is $2.2 \times 10^{-8} \text{ cm}^2/\text{s}$. By tracking the position of the NPs in fluid flow direction, the diffusion can be calculated by MSD:

$$\langle \xi(dtt) \rangle = \frac{1}{N_c} \sum_{i=1}^{N_c} \frac{1}{N} \sum_{\alpha=1}^N [x_i^\alpha(t + dtt) - x_i^\alpha(t) - V_i^\alpha dtt]^2 = 2D_x dtt \quad (24)$$

where V_i^α is the velocity of particle α at time step i , D_x is the diffusion in fluid flow direction indicated by X.

The observed MSD is a quadratic function of t since the displacement contains axial displacement term $V_i^\alpha t$, as shown in Figure 5A. To eliminate the tube flow effect on NPs distribution, Eqn. (24) is used to obtain the diffusion coefficient in x direction. By linear data fitting, average IMSD $\langle \xi(dtt) \rangle = 4.38 \times 10^{-10} \text{ cm}^2$, as indicated by a dash line in Figure 5B. Thus, the diffusion coefficient is $D_x = \frac{\langle \xi(dtt) \rangle}{2dtt} = 2.19 \times 10^{-8} \text{ cm}^2 / \text{s}$, which agrees with the theoretical value.

3.3.2 The influence of shear rate on nanoparticle delivery

The influence of different shear rates on nanoparticle delivery is considered first. The shear rate is determined by the velocity of the blood flow and vessel diameter. Typically in capillary with size between 10 and 20 μm in diameter, the mean velocity of blood flow usually ranges from 10 $\mu\text{m/s}$ to 100 $\mu\text{m/s}$ [74], and the maximum shear rate at the vessel wall ranges from 8 to 40 s^{-1} . In the simulation model, the effect of RBC tumbling motion on the dispersion of NPs under the shear rate of 8 s^{-1} and 16 s^{-1} are considered. 10 nm and 100 nm size of NPs are chose to differentiate the size effect since both are within the recommended size range (10~200 nm) of tumor drugs. A snap shot of the model is shown in Figure 6.

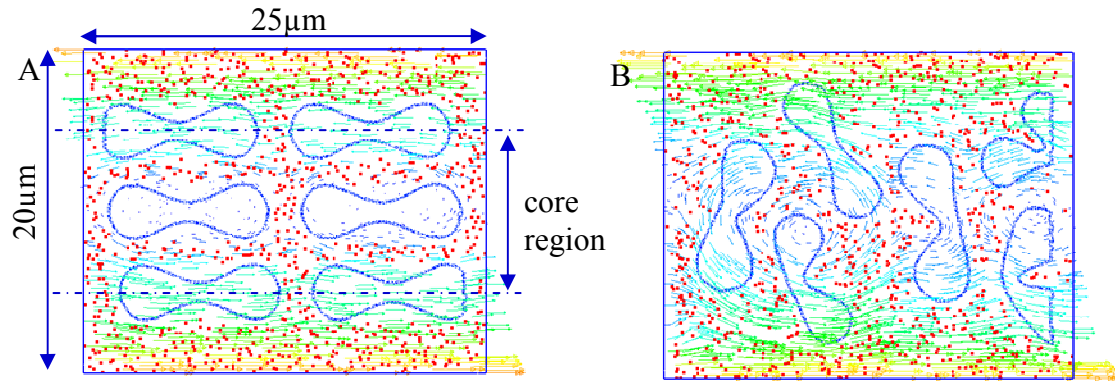


Figure 6. Simulation of RBCs and NPs interaction under a shear flow. (A) initial configuration of the model; (B) a snap shot of the model at 0.74 s.

RBC tumbling motion is found to help the dispersion of the NPs from the core region toward the edge of the simulation domain, as shown in Figure 6. Once RBCs tumble under shear flow, NPs begin to redistribute along with the motion of the RBCs. Compare to the case with pure NPs, the NP distribution when mixed with RBCs is not uniform, with more NPs in the near vessel wall region. Such non-uniform NP distribution, as shown in Figure 7, is favorable for NPs targeted binding and subsequently leads to higher NP binding efficacy. From Figure 7A, it is shown that with RBCs, the number of NPs in the edge region increases from 5% to 10%, almost doubled compared to that without RBCs. Such non-uniform NP distribution is induced by the RBCs volumetric exclusion and tumbling effect. Similar increased near-wall high particle concentration has also been reported for platelet distribution in capillary flow[77-80].

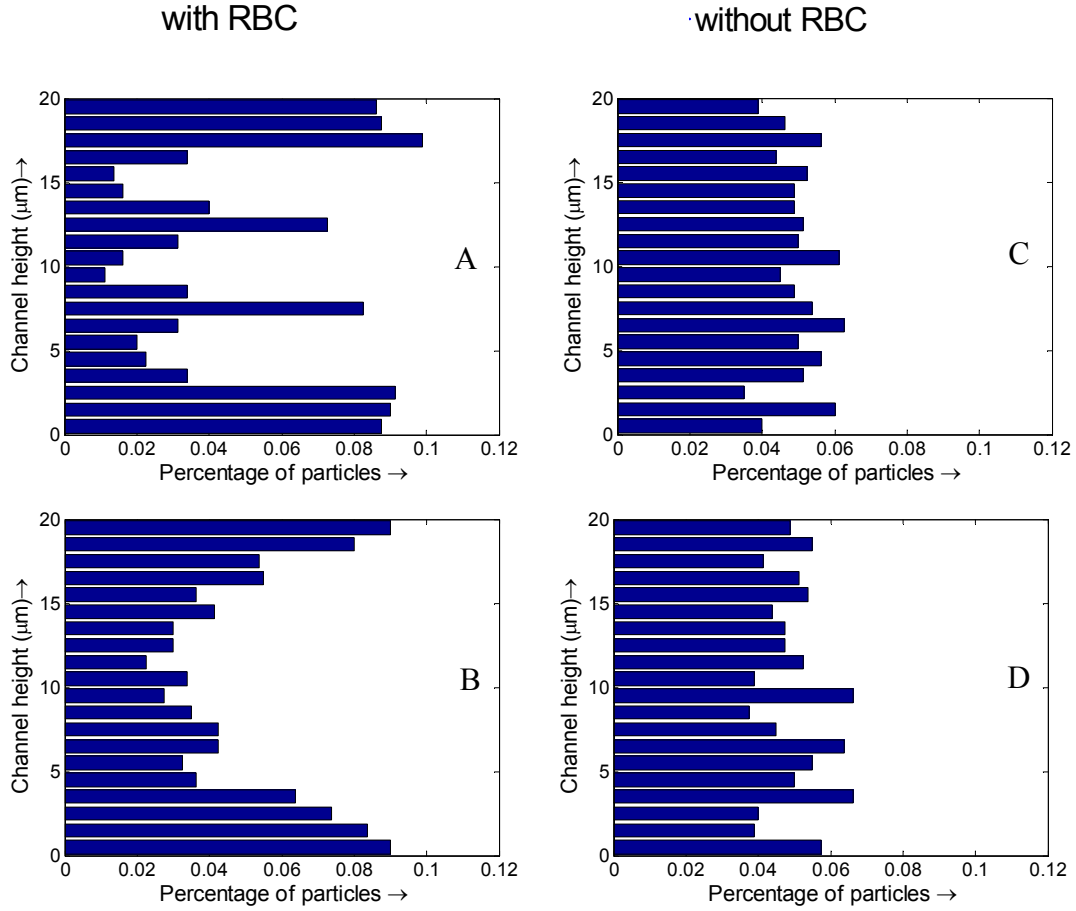


Figure 7. Nanoparticle distribution profile across the vessel. (A) initial NP distribution profile with RBCs; (B) NP distribution profile with RBCs at 1 s; (C) initial NP distribution profile without RBCs; (D) NP distribution profile without RBCs at 1 s.

Besides distribution, RBCs also influence NPs dispersion. The existence of RBCs serves as dual roles to the particle dispersion. On one hand, due to the interaction between the cells and the particles, the particles will be pushed around as RBCs tumble in the blood, thus lead to higher dispersion coefficient. For example, when 100 nm diameter NPs are introduced in the model under a shear rate of 8 s^{-1} , the average dispersion coefficient (half of the slope of the mean square displacement) is $3.6 \times 10^{-8} \text{ cm}^2/\text{s}$, a significant increase compared to the theoretical value of $2.2 \times 10^{-8} \text{ cm}^2/\text{s}$ without RBCs

considered, as shown in Figure 8A. Such enhanced dispersion is also observed by Crowl *et al.* [78] on platelet motion induced by red blood cells. On the other hand, RBCs trap particles in the space in between, especially for small NPs which diffuse faster than RBCs rotation. For example, the trapping effect for 10 nm particles is dominant during the first 0.7s when RBCs/NPs mixture are placed under a shear flow; however, the diffusion enhancement effect outweighs trapping effect once the RBCs tumbling become apparent, which is reflected in Figure 8B where the average dispersion coefficient with RBCs is $9.3 \times 10^{-8} \text{ cm}^2/\text{s}$ as compared to $6.4 \times 10^{-8} \text{ cm}^2/\text{s}$ without RBCs. It should be noted that the dispersion coefficient without RBCs is smaller than the theoretical free diffusion value $2.2 \times 10^{-7} \text{ cm}^2/\text{s}$ due to the constrained effect at the fluid channel boundaries. The zoom-in sub-plot of the MSD at the beginning (Figure 8B) shows that the dispersion coefficient is close to the theoretical value of free diffusion. To eliminate the constrained effect, the instantaneous diffusion coefficients (IDC) is calculated based on Eqn.(23). It is shown in Figure 8C that IDCs are very close to the theoretical value of NPs of corresponding size. For example, for 100 nm NPs, the IDC with RBCs is $2.22 \times 10^{-8} \text{ cm}^2/\text{s}$, while the IDC without RBCs is $2.20 \times 10^{-8} \text{ cm}^2/\text{s}$, as shown in Figure 8C. Similar results were also observed for 10 nm NPs, as shown in Figure 8D.

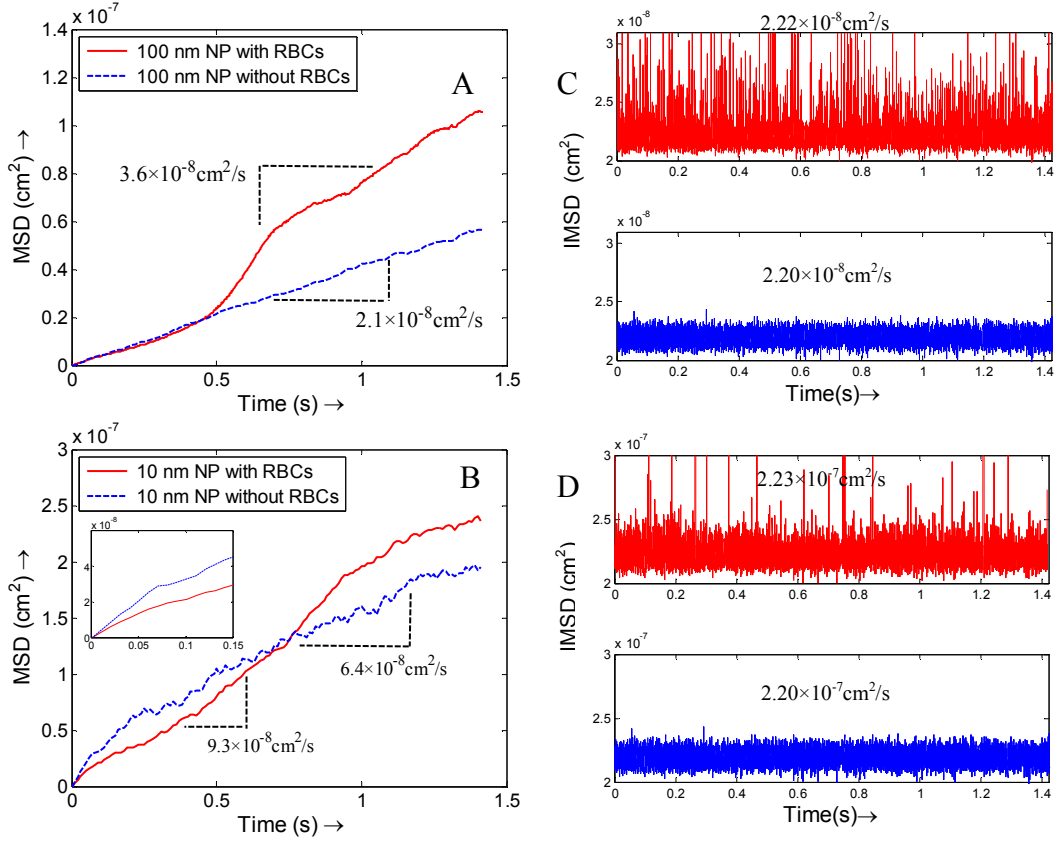


Figure 8. The overall mean square displacements (MSD) of the particles with RBCs and without RBCs under a shear rate of 8 s^{-1} , which show that RBCs enhance the dispersion for both larger NPs and smaller NPs, but in slightly different ways. (A) NPs with size of 100 nm; (B) NPs with size of 10 nm, the zoom-in subplot show smaller NPs are trapped initially by RBCs. Instantaneous mean square displacement (IMSD) of the particles with RBCs and without RBCs under shear rate of 8 s^{-1} : (C) NPs with size of 100 nm; (D) NPs with size of 10 nm.

The diffusion coefficient of particles is a physical property which usually should not change with shear rates. However, the dispersion rate might be influenced by the existence of RBCs and change with shear rates. The dispersion rate of NPs is characterized at different shear rates in our simulations. With RBCs, as the shear rate increases, the mean square displacement for NPs increases for both 100 nm and 10 nm diameter NPs, as shown in Figure 9. This is explained by the fact that RBCs tumbles

faster at higher shear rates, thus push the surrounding NPs and lead to larger dispersion. The enhancement in dispersion rate due to the existence of RBCs is more apparent for 100 nm NPs compared to 10 nm NPs. However, without RBCs, no matter how much the shear rate increases, the dispersion coefficients for NPs almost keep un-changed. Thus, larger shear rate enhances NPs dispersion due to the faster rotation of RBCs, which is favorable for NPs margination toward vessel wall surface.

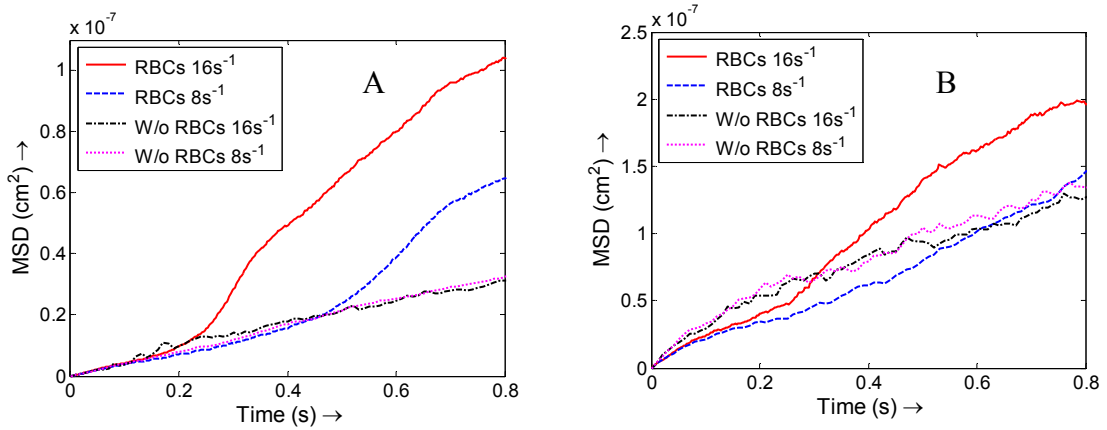


Figure 9. Mean square displacement of NPs under shear rates of 8 s^{-1} and 16 s^{-1} with RBCs and without RBCs. (A) 100 nm size of NPs; (B) 10 nm size of NPs.

3.3.3 The influence of RBCs on NP binding

NP binding dynamics involves molecular level binding between ligands coated on the NP surface and receptors on the vessel wall. The detailed binding adhesion dynamics of individual particles of arbitrary shape under various flow conditions has been studied in our previous work[81]. In this thesis, we focus on collective behavior of NPs under the influence of RBCs, thus simply bind NPs upon its contact with the wall surface. As described in Section B, the existence of RBCs lead to high near-wall NP concentration and is expected to induce faster NP binding. The NP binding dynamics is studied in a 20

μm wide vessel with the existence of RBCs under an average inlet flow rate of $20 \mu\text{m/s}$. With RBCs, the particle distribution is not uniform (see Figure 10A and B), particularly with more particles in the near vessel wall region. This non-uniform particle distribution is favorable for NPs targeted binding because with high concentration in the cell free layer region, more particles are likely to bind to the diseased area.

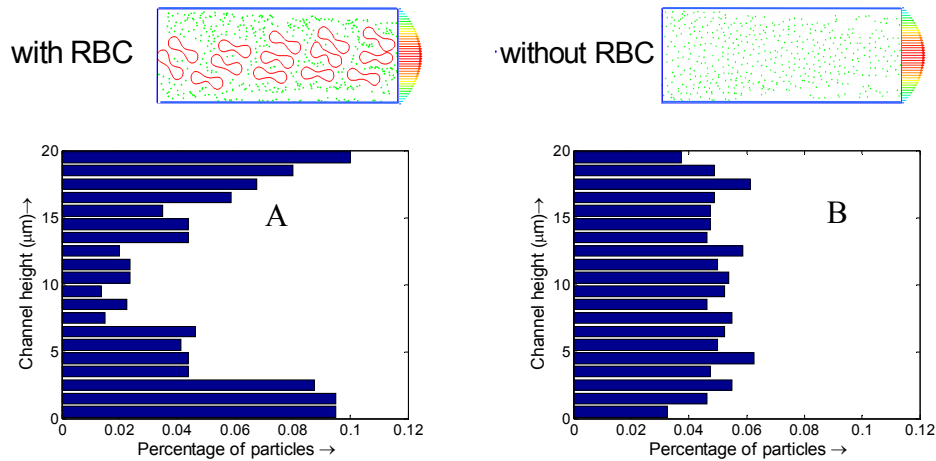


Figure 10. Particle distribution profile at time $t=7.5\text{s}$. (A) NPs with RBCs case; (B) NPs without RBCs.

The NPs binding time history is plotted in Figure 11. For the same NP concentration case, there are fewer NPs in the simulation domain, thus the total number of bounded NPs with the existence of RBCs is less than that without RBCs. However, the NPs binding rate in the initial stage with the existence of RBCs is higher than that without RBCs, as shown in Figure 11A. For the same NP dosage case, since the NP density at the near wall region is much higher than that without RBCs, NPs with RBCs bind at a significantly higher rate than that without RBCs, as shown in Figure 11B. In Figure 11, the number of bonded NPs gradually reaches a plateau, which indicates that

NP binding is a diffusion limited reaction process and the number of free NPs decreases over time.

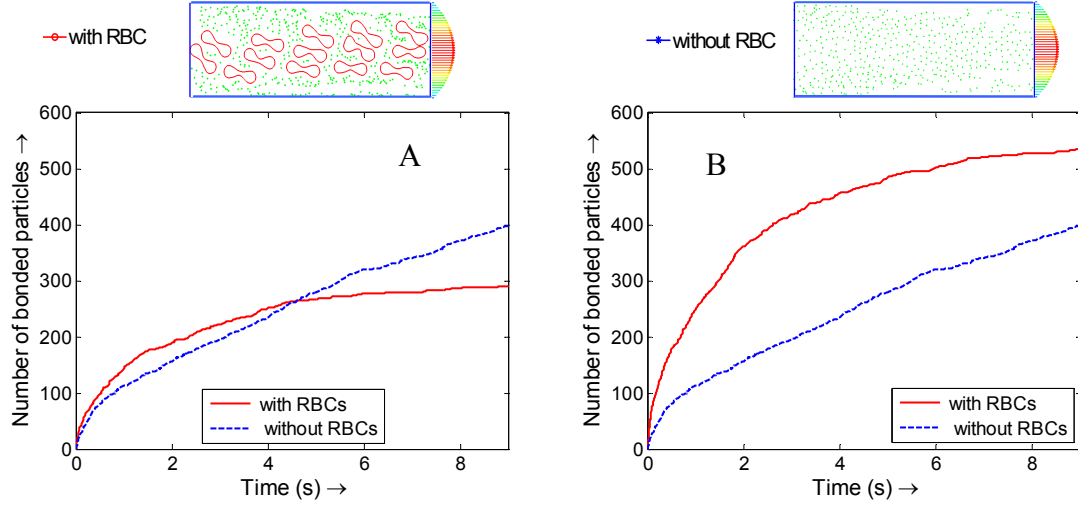


Figure 11. (A) Nanoparticle binding time histories with and without RBCs of the same effective nanoparticle density; (B) Nanoparticle binding time histories with and without RBCs of the same NP dosage.

For quantitative calculation of the binding rate, a first order reaction model is used to fit the binding curve to retrieve the binding rate:

$$\frac{\partial N_b}{\partial t} = K_f(N_0 - N_b) \quad (25)$$

where N_b is the number of bonds, N_0 is the total number of NPs in the fluid domain, K_f is the forward binding rate with units of 1/s.

The analytical solution for Eqn.(25) is $N_b = N_0(1 - \exp(-K_f t))$

However, if the bonds formation is diffusion or reaction limited, the kinematics of bonds formation is not exponential function of time. Douglas *et al.*[82] proposed to use a non-exponential reaction rate to express the bonds formation, which can be modified as:

$N_b = N_0(1 - \exp[-(K_f t)^\beta])$ where β is a parameter related to the time dependent rate.

The same method is also used by Park *et al.*[83] to fit the data of non-equilibrium NP adsorption on a model biological substrate. By fitting the data obtained in NPs binding time history, the binding rates with RBCs, without RBCs, under the same density, and under the same dosage are summarized in Figure 12.

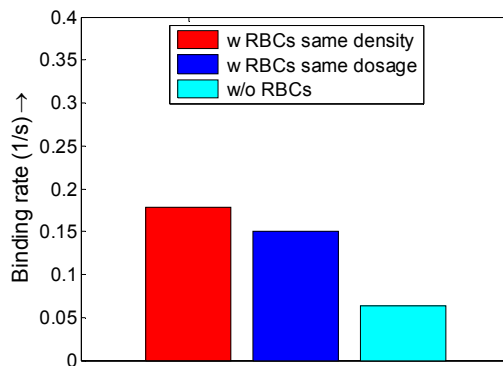


Figure 12. NPs binding rates with RBCs and without RBCs under same density and same dosage. Such increased binding rate is explained by the higher NP concentration in the cell-free-layer and larger dispersion rate.

As shown in Figure 10, with RBCs, the percentage of particles in the cell free layer increase from 5% to 10%, almost doubled compared to that without RBCs. This favorable particle distribution leads to more than two times higher binding efficacy for NPs with RBCs compared to that without RBCs, as shown in Figure 12. This higher binding rate is likely to be induced by the tumbling and blocking effect of RBCs which can help increase the NP density in the cell free layer. The particles enter the cell free layer cannot easily diffuse back to the core region of the vessel filled with RBCs. While

without RBCs, the particles are free to diffuse in any direction, thus, the binding rate decreases.

3.4 Microfluidic experimental validation

Microfluidic based blood vessel mimicking devices have been successfully developed in our lab to study NP transport and distribution[84]. To verify the results obtained in the simulation, experimental study on NPs distribution was performed by flowing 100 nm fluorescence NPs through a microfluidic channel of width 20 μm . In brief, straight 20 μm wide microfluidic channels were fabricated using standard soft lithography process[85]. The PDMS microfluidic device was bonded on clean glass slides after treating in an oxygen plasma chamber. The surface of the PDMS device was then functionalized with NeutrAvidin to bind with the biotin coated NPs. A mixture of RBCs and 100 nm biotin coated NPs with volume ratio of 36% was injected into the microfluidic device using a Harvard PHD 2000 syringe pump. The same flow rate used the simulation was chosen (20 $\mu\text{m}/\text{s}$). Channels were flushed with Phosphate Buffered Saline to remove unbound NPs from the channel after NPs distribution reached equilibrium. Imaging was done using a fluorescent microscope (Olympus IX81). After eliminating the background noise and normalizing the fluorescence intensity with the total intensity, the fluorescence intensity distribution of NPs across the channel is analyzed and plotted in Figure 13A. It is observed that the NP fluorescent intensity is higher near the channel wall compared to the core region, which is consistent with the simulated NPs distribution profile shown in Figure 13B. As a control case, flux of pure NPs without RBCs was also performed, as shown in Figure 13C. The NP fluorescent

intensity profile is flat across the channel, which again agrees with the simulation results shown in Figure 13D. It should be noted that NP fluorescent intensity is not exactly NP concentration. Due to the small size of the NPs and high flow rate, individual NPs are very hard to be visualized even with high-speed spinning disk confocal microscope. However, it is believed that NP fluorescence intensity profile essentially reflect the characteristics of the NPs distribution. Comparing the simulation and experiment data, it is concluded that RBCs can enhance the NP concentration in the margin of the vessels, thus leads to higher binding rate.

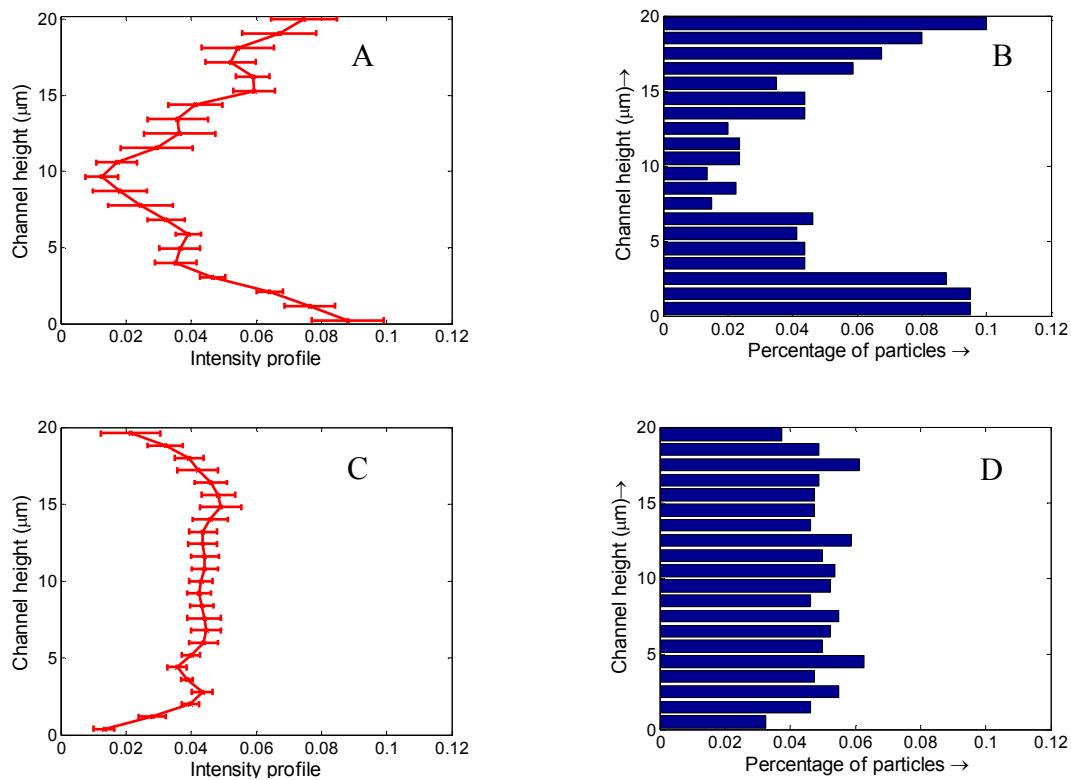


Figure 13. Fluorescence intensity across the channel in microfluidic tests, the error bar is plotted based on 10 runs of tests: (A) with RBCs; (C) without RBCs; (B) and (D): simulated NP distribution across the channel in the simulation with and without RBCs from Figure 10.

Chapter 4. Nanoparticle distribution in a vascular network

Blood vascular network consists of many generations of vessels with decreasing diameter from parents to daughters. Besides diameter, the angle between two daughters at the branch varies, which leads to different hydrodynamic conditions at each vessel trees. The angle of the bifurcation depends on the relative diameter of the daughter vessels[86]. In our model, the fluid domain contains one parent channel and two daughter channels. Both the parent and daughters are modeled as cylinders with constant diameters: 2 μm for parent channel and 1 μm for daughter channel. These small diameters are chosen because of the nanometer size of the nanoparticles which makes modeling in bigger channels computational very expensive. The characteristics of the NP distribution are mainly influenced by local shear rates, rather than channel diameter. Branched angle (defined as the angle between the center line of the parent vessel and the center line of the daughter) is chosen to be 45 degree. Due to cylindrical symmetry, the longitudinal cross section is shown in Figure 14. A rectangular region with length 3 μm and a circular region with diameter 2 μm are chosen as the representative of the straight region and branched region, respectively, as shown in the Figure 14B. The walls are set to be non-slip boundaries, the inlet is applied with a fluid velocity and the outlets are open.

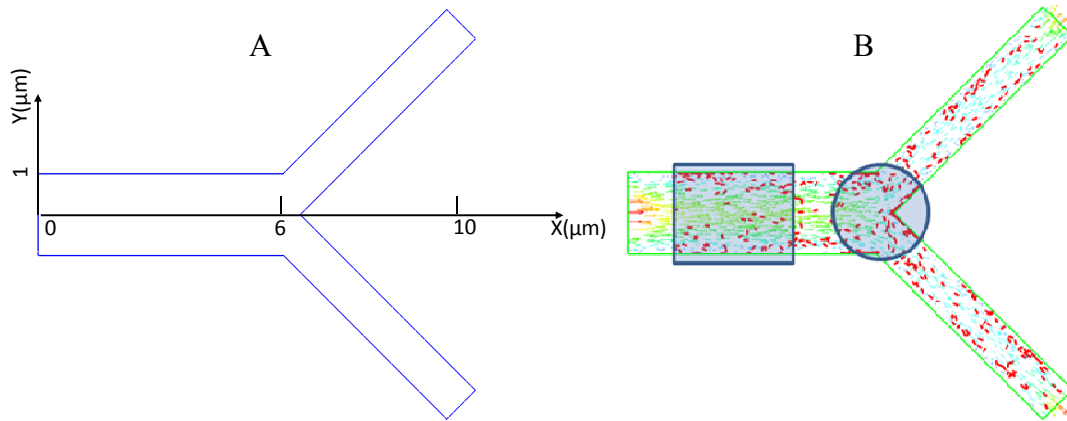


Figure 14. A bifurcation microchannel for NP deposition simulation. (A) geometry dimensions; (B) illustration of straight section and bifurcation area.

4.1 Shape dependent Nanoparticle binding dynamics

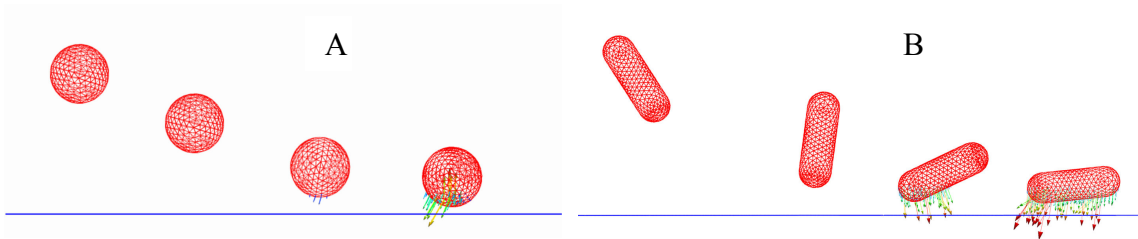


Figure 15. Trajectory snapshots of a nanosphere (A) and a nanorod (B) under shear flow. The arrows illustrate the adhesive force once the particles interact with the wall.

Under a shear flow, spheres and rods exhibit different binding behaviors. The particle shape influences both initiation of adhesion and sustained binding after adhesion.

First, initial contacts between NP and surface depend on particle shape. For spheres, their contact area is orientation irrelevant with a constant binding area; For rods, while they might have higher chance of initiating contact due to larger length and tumbling motion, rod binding is orientation dependent with varying contact area, as shown in Figure 15. Under a low shear rate, it is expected that both spheres and rods bind immediately as they contact the wall because adhesion force of a single bond is bigger

than the drag under low shear rate. At medium shear rate, the transitional contact/bind of nanorod is not enough to hold the particle and might get washed away easier compared to nanosphere. At high shear rate, the bonding force of spheres can't resist the drag force and will get washed away. In contrast, rods have a larger contact area and reduced drag force when the principle long axis is aligned with the wall, thus has higher resistance and larger adhesion probability at high shear rate.

Second, the NP shape also influences the probability of NP to stay adhered or being washed away after initial adhesion. Decuzzi *et al.* studied the adhesive strength of non-spherical particles under shear flow[28]. Assuming the particle is fixed along the surface, the attaching probability can be expressed as,

$$\frac{P_a}{m_r m_l K_a^0} = A_c \exp\left[-\frac{\lambda}{k_B T} \frac{F_{dis}}{m_r A_c}\right] \quad (26)$$

where K_a^0 is the association constant at zero load of the ligand-receptor pair; F_{dis} is the dislodging force due to hydrodynamic forces; m_r , and m_l are the receptor and ligand density respectively; A_c is contact area; λ is the characteristic length of the ligand-receptor bonds; k_B is the Boltzmann constant; and T is the temperature. From Eqn.(26), the normalized binding probability is plotted in Figure 16 with a hypothesis of 100% binding at shear rate of zero at the centroid of NPs. As shown in Figure 16, higher aspect ratio rod ($\gamma=5$) has the largest binding probability while sphere has the least binding probability. The difference becomes larger as NP size increases from 100 nm to 200 nm. It should be noted that the binding probability is based on the assumption that the long axis of nanorod is aligned with the binding surface, thus describes an equilibrium state rather than transitional state.

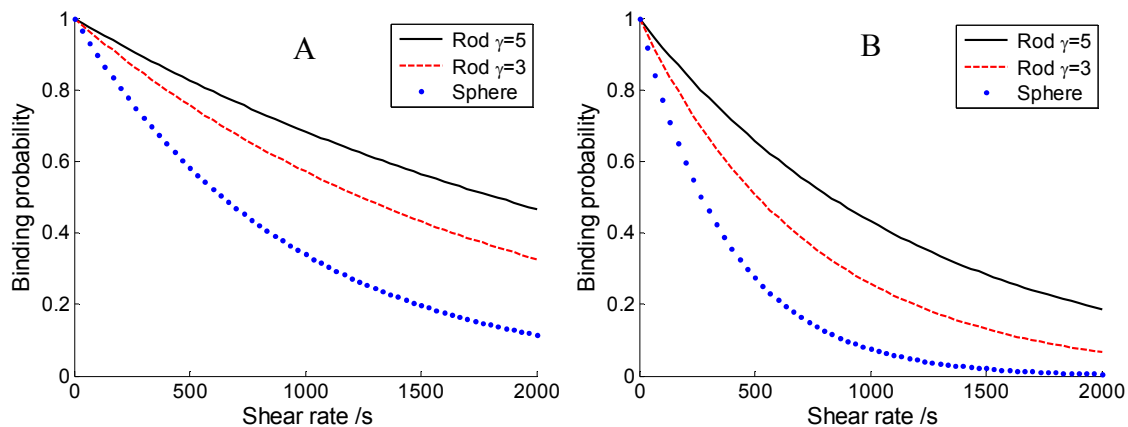


Figure 16. Normalized binding probability for (A) NP size of 100 nm; (B) NP size of 200 nm.

4.2 Distribution of Nanoparticles of different sizes

As shown in Figure 17, the deposition of particles at the bifurcation is influenced by their size. For 200 nm particles, the deposition pattern are more scattered due to the large shear force exerted by the fluid. However, for 100 nm particles, once the receptor-ligand bonds are initiated upon contact, most likely they will bind there with much less rolling, which leads to a compact binding pattern. Also, 100 nm NPs diffuse speed is about $\sqrt{2}$ times faster than 200 nm particles. So it takes more time for 200 nm NPs to bind at the wall. With the same fluid flow, the binding sites of 200 nm NPs are further than 100 nm NPs from the inlet of the channel, as indicated by the difference of starting binding sites in Figure 17.

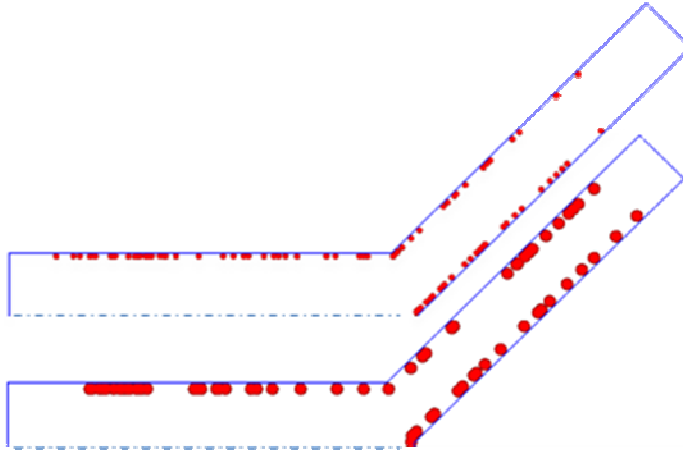


Figure 17. Distribution of nanospheres of different sizes. Half of the channel is shown in the figure due to symmetry. Top: 100 nm; Bottom: 200 nm.

4.3 Distribution of nanoparticles of different shapes and size under various shear rates

The shear rate at the vascular wall usually ranges from 250 s^{-1} to 2000 s^{-1} at capillaries[87]. To study the NP distribution under different flow conditions, simulations are performed for shear rates at the wall in the straight section of 100 s^{-1} , 200 s^{-1} , 400 s^{-1} , 600 s^{-1} , and 1000 s^{-1} , respectively. For convenience, flow rate at the inlet is used in some parts of the description since the shear rate varies at different locations of the branched channel.

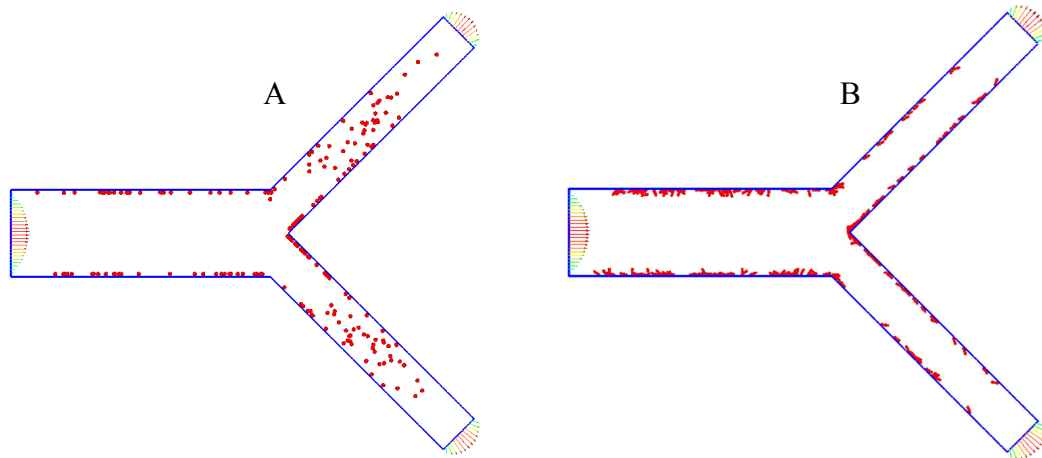


Figure 18. A snap shot of the particle distribution in the branched vessel for (A) spheres; (B) rods.

At the inlet of the vessel, 200 NPs of spheres and rods are released at the core region of the vessel, respectively. The distribution of NPs is recorded after one flow flush. Two snapshots of the NP distribution are shown in Figure 18. The binding density of 100 nm NPs over the whole channel is shown in Figure 19. There are several interesting observations in NP distribution.

First, a significant increase of particles density happens at about 6 μm distance from the inlet where the bifurcation begins. Such higher binding density at branched region applies to all cases simulated except for the sphere at the highest flow rate of 500 $\mu\text{m/s}$, which has 1000 s^{-1} shear rate at straight channel and 2000 s^{-1} shear rate at branched region, as shown in Figure 19E. The flow is deviated at the bifurcation point, which leads to a higher opportunity for NP to initiate contact with the channel wall. Figure 19E implies that the bonding force for spheres cannot resist the drag force from the blood at such high shear rate. The shear rate at the bifurcation is as high as 2000 s^{-1} , which corresponds to an adhesion probability of around 15%, as shown in Figure 16A.

Second, NP binding rate decreases as shear rate increases. This is indicated by the decrease of the total number of bonded particles along the fluid channel from Figure A to E. Higher shear rate increases the drag force exerted on the NP, thus leading to low binding. This observation is consistent with theoretical prediction shown in Figure 16 and other experimental observations [88-89].

Third, high aspect ratio rod shows higher binding density at low shear rates (Figure A-C), and lower binding density at higher shear rates (Figure 19D-E). This is quite counterintuitive and different from the theoretical prediction shown in Figure 16. This might be induced by the competence between drag force and bonding force. At low shear rate, the binding force from a few ligand-receptor bonds is large enough to hold the particles. Nanorod has higher chance of contact with the wall, thus higher binding. However, in high shear rate, the drag force exerted on the NPs depends on the orientation of the NPs. For example, if a rod has a point contact with the wall, it is subjected to a larger drag and smaller adhesion force, and gets drifting away easily. If it is in contact the wall aligned with its long axis, it may stay bonded with the wall due to the larger adhesion force and smaller drag force. This concept is clearly illustrated in Figure 20 through the snap shots of a sphere and a rod during the dynamics binding process.

Another interesting observation is the dynamic shifting in distribution of NPs at different shear rates. As the flow rate increases, the particle binding distribution tends to shift toward downstream, as indicated by the dash dark lines marking the peak of distribution. More particles are bonded in the downstream, e.g., the particle density at 8 μm changes from 0 at 50 $\mu\text{m/s}$ to 4 at 300 $\mu\text{m/s}$. At high shear rates, NP cannot bind firmly upon contact with the wall. Due to the tethering effect of receptor-ligand bonds,

NP keeps rolling and tumbling along the surface until the adhesion force outweighs the drag force. Although some NPs will bind in the end, the final binding sites are different from their initial contact sites.

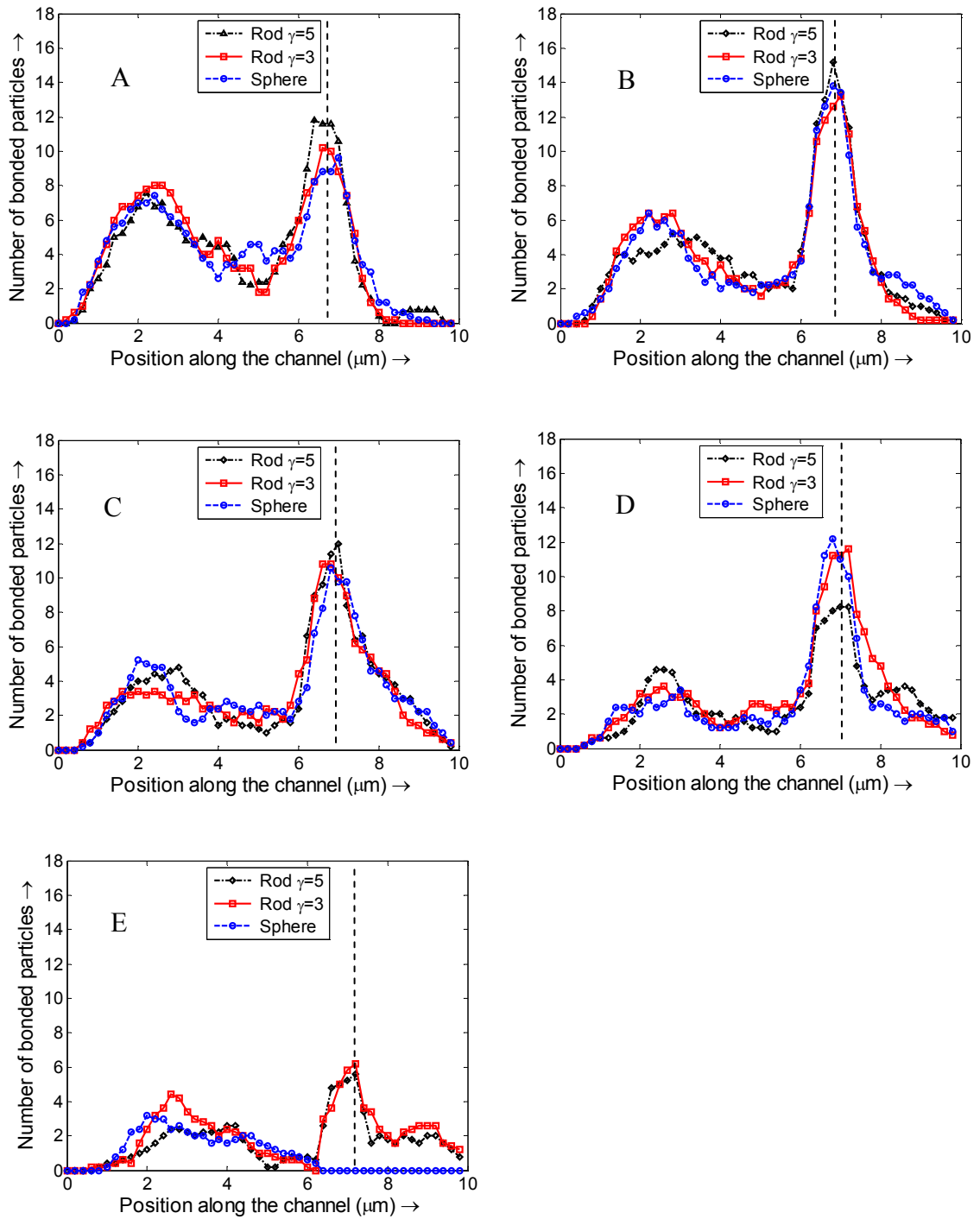


Figure 19. 100 nm nanoparticle distribution along the channel .(A)50 μm /s, (B)100 μm /s,(C) 200 μm /s,(D) 300 μm /s,(E) 500 μm /s.

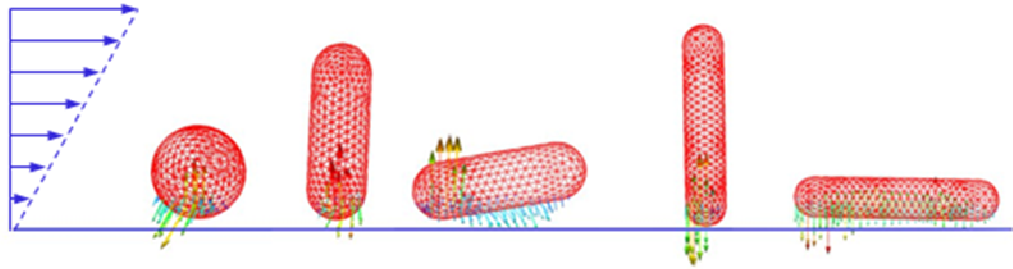


Figure 20. Adhesion of NPs depends on particle shape and their orientation. Nanorods have smaller contact area and bonding force during transient rotation, but maximal bonding force after laying down with long axis aligned with wall .

NPs of 200 nm are also simulated to study how NP size changes its distribution. The distributions of 200 nm NPs over different shear rates are shown in Figure 21. Compared to 100 nm case shown in Figure 19, the total number of bonded NPs decreases with increased size. At low shear rate, the NPs distribution is more non-uniform for 200 nm NPs compared to 100 nm NPs, with more NPs deposited at the bifurcation region. At the shear rate increases, the detachment of particles begins to happen at the bifurcation region. For example, detachment of spheres begins to happen at $200 \mu\text{m/s}$, which is lower than the 100 nm case. This is because larger NPs experience larger drag force at the same shear rate, thus are easier to be detached. At the high flow rate of $300 \mu\text{m/s}$, most spheres are unable to bind. At the highest flow rate of $500 \mu\text{m/s}$, only rods with high aspect ratio of 5 are able to bind onto the wall. The binding density for both nanorod and nanosphere decreases over increased flow rate.

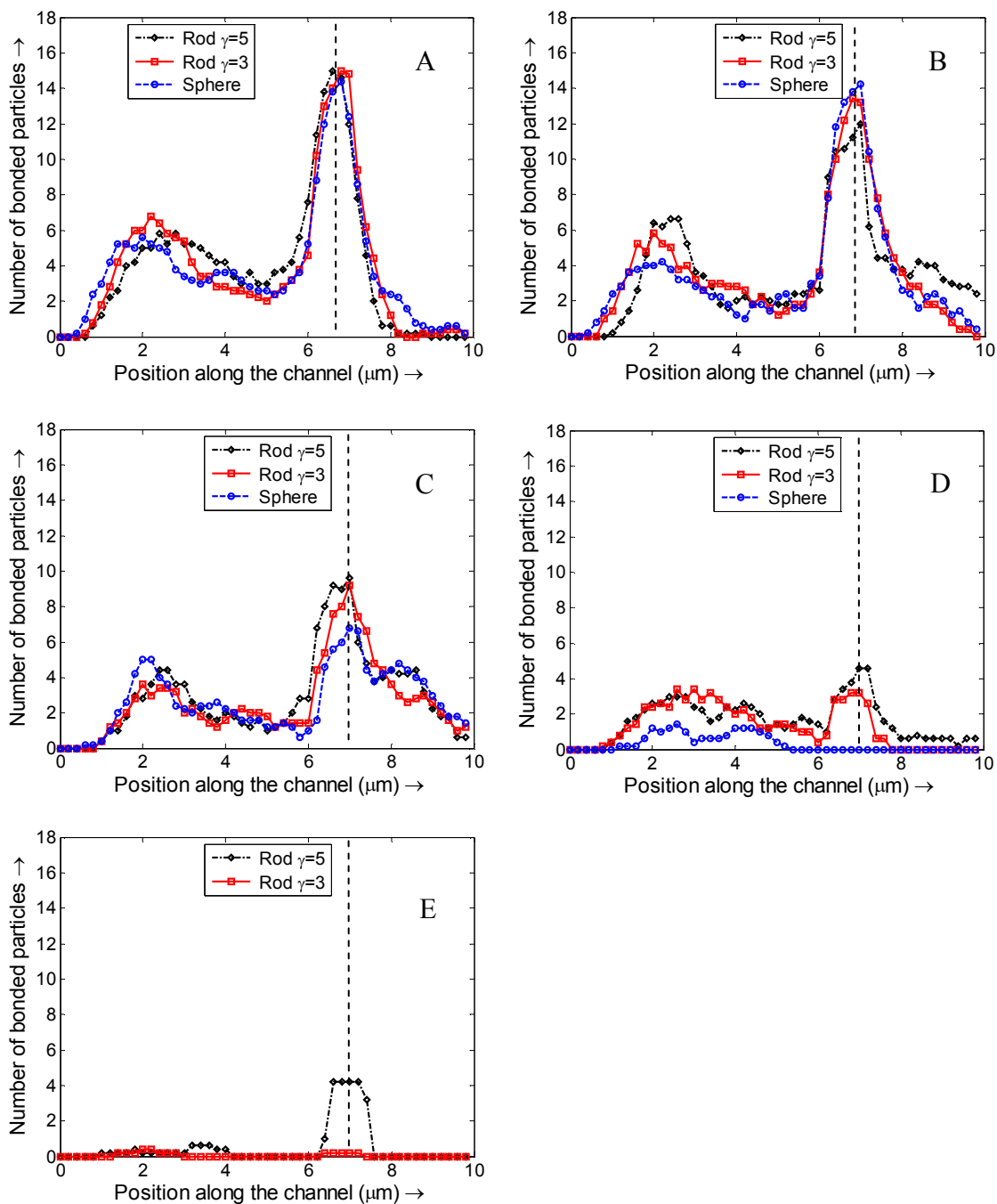


Figure 21. 200 nm Nanoparticle distribution along the channel .(A)50 μm/s, (B)100 μm/s, (C) 200 μm/s,(D) 300 μm/s,(E) 500 μm/s.

4.4 Influence of Péclet number on Nanoparticle distribution pattern

While adhesion plays an important role in NP binding after contact, the initialization of NP contact with wall is mainly determined by convection and diffusion. The fraction of NPs deposited on the straight section and the branched region is influenced by flow rate, NP diffusion speed and channel size, which could be characterized by the Péclet number (***Pe***) defined as:

$$Pe = \frac{LU}{D} \quad (27)$$

where L is the characteristic length of the channel, U is the average fluid velocity, and D is the NP diffusion coefficient. In our model, L is chosen as 1 μm , D is calculated from Stokes-Einstein equation as $4.4 \times 10^{-12} \text{ m}^2/\text{s}$ and $2.2 \times 10^{-12} \text{ m}^2/\text{s}$ for 100 nm and 200 nm NPs, respectively.

To characterize the NP distribution, the ratio between the number of deposited NPs in branched region and straight section is plotted as a function of Péclet number. As shown in Figure 22. When Péclet number is small, diffusion is dominant so that most NPs bind at the straight section. As the Péclet number increases, convection becomes dominant, leading to higher binding density at the branched region. However, the ratio reaches peak first and then decreases as Péclet number increases. This is because higher Péclet number means higher flow speed, which makes NP difficult to marginate toward wall. Shape also influences the distribution ratio. Spheres reach the peak ratio at the smallest Péclet number, followed by rod-shaped NPs with aspect ratio $\gamma=3$, while NPs with aspect ratio $\gamma=5$ have the peak ratio latest.

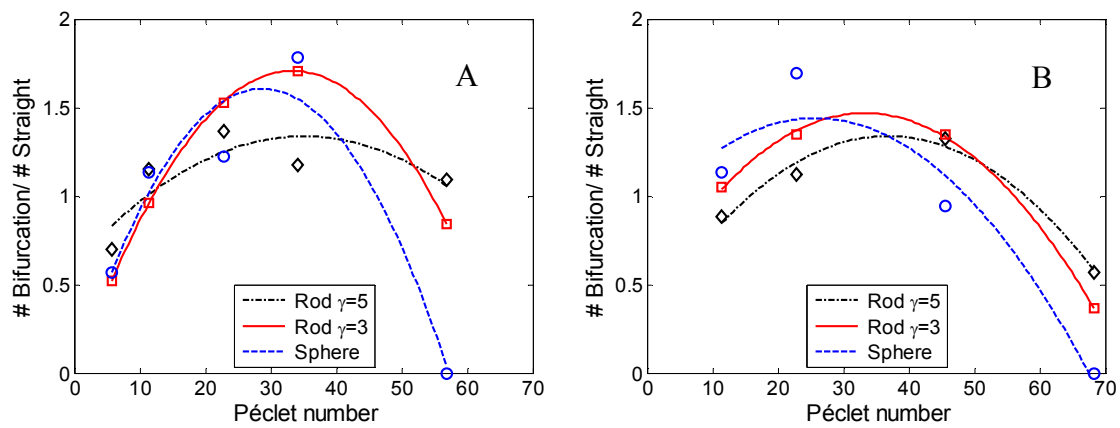


Figure 22. Ratio of the number of deposited NPs on branched region and straight section depends on the Péclet number. The simulation data are fitted by quadratic lines through least square method. (A) 100 nm NPs; (B) 200 nm NPs.

Chapter 5. Conclusion and Future work

In summary, a particle-cell hybrid model is developed to model nanoparticles transport, dispersion, and adhesion in blood stream through coupled Immersed Finite Element method and particle Brownian adhesion dynamics. The dispersion and adhesion kinetics of NPs in microcirculation is studied for the first time with cell hydrodynamics coupled with particle Brownian dynamics. The adhesion kinetics of NPs is found to be significantly influenced by the existence of RBCs and shear rates. The cell-free-layer and NP-cell interaction largely influence both the dispersion and binding rates, thus impact targeted delivery efficacy. Under a shear flow, the RBCs' tumbling motion will enhance NP dispersion. NP dispersion rate increases with shear rate. The distribution of NPs in capillary flow is not uniform, with more particles near the vessel wall surface. Such margination of NPs occurs due to hydrodynamic interaction rather than RBCs volumetric exclusion effect. Higher density of NPs in the near-wall region leads to higher binding rate for NPs in 20 μm capillaries. The binding rate of NPs with RBCs is two times of that without RBCs. This observation is applicable to NPs of various sizes from 10 nm to 200 nm.

From the branched vessels model, it is observed that NPs with smaller size bind fast than bigger ones. This is because diffusion coefficient is proportional to the inverse of particle size, thus diffusion speed for 100 nm particles is $\sqrt{2}$ times faster than 200 nm particles. Meanwhile, larger particles are subjected to larger drag force from fluid flow, which lead to lower binding probability. This conclusion is consistent with the statement that the critical shear stress required to remove adhered particles decreases as particles

size increases[90]. The binding dynamics of rod-shaped NPs is initial contact and orientation dependent. Rod shaped NPs with larger aspect ratio do not necessarily have higher binding rate. This observation is quite different from the prediction from theoretical model[28]. One assumption made in the theoretical model is that the long axis of non-spherical particles is aligned with the contact wall, which ensures the largest adhesion force with maximal contact area. However, such idealized binding configuration does not always occur *in vivo*. Such counter-intuitive finding is consistent with other group's simulation results which state that the interaction between NPs and cells is particle initial contact orientation and local curvature dependent at the contact site[91]. Moreover, NP bond formation depends on the balance between adhesion and drag force. The drag force increases linearly with shear rate resulting in lower binding probability of NPs at higher shear rate. The diverging flow at vessel bifurcations enables particles to have larger binding propensity. Furthermore, the percentage of NPs binding to the straight section and bifurcation region is found to be a function of Péclet number. When Péclet number is small, diffusion is dominant, thus more particles are deposited at the straight section. As Péclet number increases, convection dominates over diffusion so that more particles are transported and deposited to the bifurcation region. For even larger Péclet number, the shear stress at the wall surpasses the critical shear stress for stable NP binding, leading to detachment of NPs. Results from this study contribute to the fundamental understanding and knowledge on how the particulate nature of blood influences NP delivery, which will provide mechanistic insights on the nanomedicine design for targeted drug delivery applications.

It should be noted that in our model, the particle distribution is studied at microscale where motion of individual particle is tracked and the binding dynamics is described with details of ligand-receptor bonds. However, to predict large scale overall *in vivo* distribution, a higher scale continuum model is required to characterize NP convection, diffusion and reaction. In the continuum model, particle binding will be described in terms of NP concentration, diffusion coefficient, shear rates, reaction rates, etc. How to link the microscale particulate model with the continuum model will be an interesting topic to explore in the future. A multiscale model consisting of continuum model of organ level and particulate model of cellular level will be beneficial to NP distribution prediction and drug dosage administration. It is very important to develop a personalized drug delivery prediction tool. Both doctors and patients will be happy if they know where the drug goes and the minimal drug dosage to fight against the disease beforehand. For example, based on the magnetic resonance imaging (MRI) of a patient, an organ level of vasculature network can be reconstructed and input into computational model. Specific physiological conditions can be applied to the model to accurately simulate the drug transport. Mathematical modeling of drug delivery in patient specific coronary artery walls has been done by J.R. Hughes[92].

However, the large scale model will present more challenges to the researchers. Nowadays, super computers can handle the whole model with many generations of vessels, blood components, and drugs. Millions of elements can be loaded and processed by fast computers. The bottleneck is how to develop an algorithm that scales well on millions of heterogeneous cores. Some pioneering works have been done to face this grand challenge. For example, Dr. Margetts did a lot of work in parallel finite element

analysis[93], particularly in solving Navier-Stokes equations. Fast algorithms for simulating the dynamics of vesicles suspended in 3D flow has been studied recently[94] and can be extended to model RBCs, platelets, and particles in large scale blood flow.

Based on aforementioned discussion, the future work based on this thesis is listed below:

- 1) Create a multiscale model that can link the nanoscale NP reaction model to continuum scale model. We hope we can obtain continuum scale parameters such as adhesion and detaching rates directly from the nanoscale model.

- 2) Extend the current code into a parallel one, which requires to design the algorithm from the parallelization point of view. Specifically, it has several capabilities: first, it can make the code run faster with a full use of the currently available computing resources; second, it will enable us to model large scale drug delivery in vascular geometry based on scanned MRI images, since fast algorithm can handle more complex and challenge computing within a reasonable time.

- 3) Verify and validate the simulation results through microfluidic experiments in mimetic blood vessels. The mathematical tool for NP binding and distribution prediction will be more meaningful if the control experiments can validate the computational results.

Reference

1. Wang, T., et al., *Cytoplasmic Delivery of Liposomes into MCF-7 Breast Cancer Cells Mediated by Cell-Specific Phage Fusion Coat Protein*. MOLECULAR PHARMACEUTICS, 2010. **7**(4): p. 1149-1158.
2. Al-Jamal, W.T. and K. Kostarelos, *Liposomes: From a Clinically Established Drug Delivery System to a Nanoparticle Platform for Theranostic Nanomedicine*. Accounts of Chemical Research, 2011. **44**(10): p. 1094-1104.
3. Choudhury, R.P., V. Fuster, and Z.A. Fayad, *Molecular, cellular and functional imaging of atherothrombosis*. Nature Reviews Drug Discovery, 2004. **3**(11): p. 913-925.
4. Maysinger, D., et al., *Fate of micelles and quantum dots in cells*. Eur J Pharm Biopharm, 2007. **65**(3): p. 270-81.
5. Sutton, D., et al., *Functionalized micellar systems for cancer targeted drug delivery*. Pharm Res, 2007. **24**(6): p. 1029-46.
6. Torchilin, V.P., *Targeted polymeric micelles for delivery of poorly soluble drugs*. Cell Mol Life Sci, 2004. **61**(19-20): p. 2549-59.
7. Gao, X., et al., *In vivo molecular and cellular imaging with quantum dots*. Curr Opin Biotechnol, 2005. **16**(1): p. 63-72.
8. Smith, A.M., et al., *Engineering luminescent quantum dots for in vivo molecular and cellular imaging*. Ann Biomed Eng, 2006. **34**(1): p. 3-14.
9. Koenig, S. and V. Chechik, *Shell cross-linked Au nanoparticles*. Langmuir, 2006. **22**(11): p. 5168-73.
10. Lou, X., C. Wang, and L. He, *Core-shell Au nanoparticle formation with DNA-polymer hybrid coatings using aqueous ATRP*. Biomacromolecules, 2007. **8**(5): p. 1385-90.
11. Yang, Y., et al., *Template guided self-assembling two-dimensional array of Au@SiO₂ core-shell nanoparticles for room-temperature single electron transistors*. J Nanosci Nanotechnol, 2005. **5**(2): p. 179-83.
12. Cheng, Y., et al., *Dendrimer-based prodrugs: design, synthesis, screening and biological evaluation*. Comb Chem High Throughput Screen, 2007. **10**(5): p. 336-49.
13. Duncan, R. and L. Izzo, *Dendrimer biocompatibility and toxicity*. Adv Drug Deliv Rev, 2005. **57**(15): p. 2215-37.
14. Najlah, M. and A. D'Emanuele, *Crossing cellular barriers using dendrimer nanotechnologies*. Curr Opin Pharmacol, 2006. **6**(5): p. 522-7.
15. Roy, I., et al., *Ceramic-Based Nanoparticles Entrapping Water-Insoluble Photosensitizing Anticancer Drugs: A Novel Drug-Carrier System for Photodynamic Therapy*. Journal of the American Chemical Society, 2003. **125**(26): p. 7860-7865.
16. Harisinghani, M.G., et al., *Noninvasive Detection of Clinically Occult Lymph-Node Metastases in Prostate Cancer*. New England Journal of Medicine, 2003. **348**(25): p. 2491-2499.

17. Weissleder, R., et al., *Ultrasmall superparamagnetic iron oxide: characterization of a new class of contrast agents for MR imaging*. *Radiology*, 1990. **175**(2): p. 489-493.
18. Cogley, C.M., et al., *Targeting gold nanocages to cancer cells for photothermal destruction and drug delivery*. *Expert Opinion on Drug Delivery*, 2010. **7**(5): p. 577-587.
19. Huang, X., et al., *Cancer Cell Imaging and Photothermal Therapy in the Near-Infrared Region by Using Gold Nanorods*. *Journal of the American Chemical Society*, 2006. **128**(6): p. 2115-2120.
20. Sardar, R. and J.S. Shumaker-Parry, *Asymmetrically Functionalized Gold Nanoparticles Organized in One-Dimensional Chains*. *Nano Letters*, 2008. **8**(2): p. 731-736.
21. Park, J.-H., et al., *Systematic Surface Engineering of Magnetic Nanoworms for In vivo Tumor Targeting*. *Small*, 2009. **5**(6): p. 694-700.
22. Dai, Q., et al., *A "Nanonecklace" Synthesized from Monofunctionalized Gold Nanoparticles*. *Journal of the American Chemical Society*, 2005. **127**(22): p. 8008-8009.
23. Geng, Y., et al., *Shape effects of filaments versus spherical particles in flow and drug delivery*. *Nat Nanotechnol*, 2007. **2**(4): p. 249-55.
24. Chen, H.Y., et al., *Controlled assembly of eccentrically encapsulated gold nanoparticles*. *Journal of the American Chemical Society*, 2008. **130**(36): p. 11858-11859.
25. Dormidontova, E.E. and H. Djohari, *Kinetics of Nanoparticle Targeting by Dissipative Particle Dynamics Simulations*. *Biomacromolecules*, 2009. **10**(11): p. 3089-3097.
26. Gref, R., et al., *Biodegradable long-circulating polymeric nanospheres*. *Science*, 1994. **263**(5153): p. 1600-1603.
27. Pasqualini, R. and E. Ruoslahti, *Organ targeting In vivo using phage display peptide libraries*. *Nature*, 1996. **380**(6572): p. 364-366.
28. Decuzzi, P. and M. Ferrari, *The adhesive strength of non-spherical particles mediated by specific interactions*. *Biomaterials*, 2006. **27**(30): p. 5307-14.
29. Decuzzi, P., et al., *A theoretical model for the margination of particles within blood vessels*. *Annals of Biomedical Engineering*, 2005. **33**(2): p. 179-190.
30. Decuzzi, P., et al., *Adhesion of microfabricated particles on vascular endothelium: A parametric analysis*. *Annals of Biomedical Engineering*, 2004. **32**(6): p. 793-802.
31. Shipley, R.J. and S.J. Chapman, *Multiscale Modelling of Fluid and Drug Transport in Vascular Tumours*. *Bulletin of Mathematical Biology*, 2010. **72**(6): p. 1464-1491.
32. Modok, S., et al., *Transport kinetics of four-coordinate and six-coordinate platinum compounds in the multicell layer tumour model*. *British Journal of Cancer*, 2007. **97**(2): p. 194-200.
33. Mahmoudi, M., et al., *Multiphysics Flow Modeling and in Vitro Toxicity of Iron Oxide Nanoparticles Coated with Poly(vinyl alcohol)*. *The Journal of Physical Chemistry C*, 2009. **113**(6): p. 2322-2331.

34. Li, X.L., K.L. Yao, and Z.L. Liu, *CFD study on the magnetic fluid delivering in the vessel in high-gradient magnetic field*. Journal of Magnetism and Magnetic Materials, 2008. **320**(11): p. 1753-1758.
35. Liu, Y., R.M.C. So, and C.H. Zhang, *Modeling the bifurcating flow in a human lung airway*. Journal of Biomechanics, 2002. **35**(4): p. 465-473.
36. Zhang, Z. and C. Kleinstreuer, *Airflow structures and nano-particle deposition in a human upper airway model*. Journal of Computational Physics, 2004. **198**(1): p. 178-210.
37. Doshi, N., et al., *Flow and adhesion of drug carriers in blood vessels depend on their shape: A study using model synthetic microvascular networks*. Journal of Controlled Release, 2010. **146**(2): p. 196-200.
38. <http://www.sciencedaily.com/releases/2007/07/070709171558.htm>.
39. Einstein, A., *Investigations on the Theory of Brownian Movement*. 1956: New York: Dover.
40. Ermak, D.L. and J.A. Mccammon, *Brownian Dynamics with Hydrodynamic Interactions*. Journal of Chemical Physics, 1978. **69**(4): p. 1352-1360.
41. Li, A. and G. Ahmadi, *Dispersion and Deposition of Spherical-Particles from Point Sources in a Turbulent Channel Flow*. Aerosol Science and Technology, 1992. **16**(4): p. 209-226.
42. Sharma, N. and N.A. Patankar, *Direct numerical simulation of the Brownian motion of particles by using fluctuating hydrodynamic equations*. Journal of Computational Physics, 2004. **201**(2): p. 466-486.
43. Mody, N.A. and M.R. King, *Influence of Brownian motion on blood platelet flow behavior and adhesive dynamics near a planar wall*. Langmuir, 2007. **23**(11): p. 6321-8.
44. Mori, N., M. Kumagae, and K. Nakamura, *Brownian dynamics simulation for suspensions of oblong-particles under shear flow*. Rheologica Acta, 1998. **37**(2): p. 151-157.
45. Bell, G., *Models for the specific adhesion of cells to cells*. Science, 1978. **200**(4342): p. 618-627.
46. Bell, G.I., M. Dembo, and P. Bongrand, *Cell adhesion. Competition between nonspecific repulsion and specific bonding*. Biophysical Journal, 1984. **45**(6): p. 1051-1064.
47. Ward, M.D. and D.A. Hammer, *A theoretical analysis for the effect of focal contact formation on cell-substrate attachment strength*. Biophysical Journal, 1993. **64**(3): p. 936-959.
48. Cozens-Roberts, C., D.A. Lauffenburger, and J.A. Quinn, *Receptor-mediated cell attachment and detachment kinetics. I. Probabilistic model and analysis*. Biophysical journal, 1990. **58**(4): p. 841-856.
49. Liu, Y.L. and W.K. Liu, *Rheology of red blood cell aggregation by computer simulation*. Journal of Computational Physics, 2006. **220**(1): p. 139-154.
50. Liu, Y.L., et al., *Coupling of Navier-Stokes equations with protein molecular dynamics and its application to hemodynamics*. International Journal for Numerical Methods in Fluids, 2004. **46**(12): p. 1237-1252.

51. Skalak, R., et al., *Mechanics of Rouleau Formation*. Biophysical Journal, 1981. **35**(3): p. 771-781.
52. Eggleton, C.D. and A.S. Popel, *Large deformation of red blood cell ghosts in a simple shear flow*. Physics of Fluids, 1998. **10**(8): p. 1834-1845.
53. Pozrikidis, C., *Numerical simulation of the flow-induced deformation of red blood cells*. Annals of Biomedical Engineering, 2003. **31**(10): p. 1194-1205.
54. Zhang, L., et al., *Immersed finite element method*. Computer Methods in Applied Mechanics and Engineering, 2004. **193**(21-22): p. 2051-2067.
55. Liu, W.K., et al., *Immersed finite element method and its applications to biological systems*. Computer Methods in Applied Mechanics and Engineering, 2006. **195**(13-16): p. 1722-1749.
56. Liu, W.K., D.W. Kim, and S.Q. Tang, *Mathematical foundations of the immersed finite element method*. Computational Mechanics, 2007. **39**(3): p. 211-222.
57. Liu, Y., et al., *Immersed electrokinetic finite element method*. International Journal for Numerical Methods in Engineering, 2007. **71**(4): p. 379-405.
58. Peskin, C.S. and D.M. McQueen, *A 3-Dimensional Computational Method for Blood-Flow in the Heart .I. Immersed Elastic Fibers in a Viscous Incompressible Fluid*. Journal of Computational Physics, 1989. **81**(2): p. 372-405.
59. Peskin, C.S. and D.M. McQueen, *Modeling Prosthetic Heart-Valves for Numerical-Analysis of Blood-Flow in the Heart*. Journal of Computational Physics, 1980. **37**(1): p. 113-132.
60. Peskin, C.S., *The immersed boundary method*. Acta Numerica, 2002. **11**: p. 479-517.
61. Saad, Y. and M.H. Schultz, *Gmres - a Generalized Minimal Residual Algorithm for Solving Nonsymmetric Linear-Systems*. Siam Journal on Scientific and Statistical Computing, 1986. **7**(3): p. 856-869.
62. AlMomani, T., et al., *Micro-scale Dynamic Simulation of Erythrocyte-Platelet Interaction in Blood Flow*. Annals of Biomedical Engineering, 2008. **36**(6): p. 905-920.
63. Arie L. Edelstein, N.A., *Brownian simulation of many-particle binding to a reversible receptor array*. Journal of Computational Physics, 1997. **132**: p. 260-275.
64. Breedveld, V., et al., *The measurement of the shear-induced particle and fluid tracer diffusivities in concentrated suspensions by a novel method*. Journal of Fluid Mechanics, 1998. **375**: p. 297-318.
65. Marchioro, M. and A. Acrivos, *Shear-induced particle diffusivities from numerical simulations*. Journal of Fluid Mechanics, 2001. **443**: p. 101-128.
66. Wang, Y., R. Mauri, and A. Acrivos, *The transverse shear-induced liquid and particle tracer diffusivities of a dilute suspension of spheres undergoing a simple shear flow*. Journal of Fluid Mechanics, 1996. **327**: p. 255-272.
67. Boryczko, K., W. Dzwiniel, and D. A. Yuen, *Dynamical clustering of red blood cells in capillary vessels*. Journal of Molecular Modeling, 2003. **9**(1): p. 16-33.
68. Wang, J., et al., *More Effective Nanomedicines through Particle Design*. Small, 2011. **7**(14): p. 1919-1931.

69. Petros, R.A. and J.M. DeSimone, *Strategies in the design of nanoparticles for therapeutic applications*. Nat Rev Drug Discov, 2010. **9**(8): p. 615-627.
70. Alexis, F., et al., *Factors Affecting the Clearance and Biodistribution of Polymeric Nanoparticles*. MOLECULAR PHARMACEUTICS, 2008. **5**(4): p. 505-515.
71. Farokhzad, O.C., et al., *Targeted nanoparticle-aptamer bioconjugates for cancer chemotherapy in vivo*. Proceedings of the National Academy of Sciences, 2006. **103**(16): p. 6315-6320.
72. Win, K.Y. and S.-S. Feng, *In vitro and in vivo studies on vitamin E TPGS-emulsified poly(d,l-lactic-co-glycolic acid) nanoparticles for paclitaxel formulation*. Biomaterials, 2006. **27**(10): p. 2285-2291.
73. Pandey, R., et al., *Nanoparticle encapsulated antitubercular drugs as a potential oral drug delivery system against murine tuberculosis*. Tuberculosis, 2003. **83**(6): p. 373-378.
74. Decuzzi, P. and M. Ferrari, *The adhesive strength of non-spherical particles mediated by specific interactions*. Biomaterials, 2006. **27**(30): p. 5307-5314.
75. Lee, J.-H., et al., *Effective viscosities and thermal conductivities of aqueous nanofluids containing low volume concentrations of Al₂O₃ nanoparticles*. International Journal of Heat and Mass Transfer, 2008. **51**(11-12): p. 2651-2656.
76. Taylor, G., *Dispersion of Soluble Matter in Solvent Flowing Slowly through a Tube*. Proceedings of the Royal Society of London, Series A-Mathematical and Physical Science, 1953. **219**(1137): p. 186-203.
77. Bea Woldhuis, G.-J.T., *concentration profile of blood platelets differs in arterioles and venules*. American Journal of Physiology-Heart and Circulatory Physiology, 1992. **262**(4): p. H1217-H1223.
78. Crowl, L.M. and A.L. Fogelson, *Computational model of whole blood exhibiting lateral platelet motion induced by red blood cells*. International Journal for Numerical Methods in Biomedical Engineering, 2010. **26**(3-4): p. 471-487.
79. R. Zhao, J.N.M., J.F. Antaki, *Drag-reducing polymers diminish near-wall concentration of platelets in microchannel blood flow*. Biorheology, 2011. **47**(3-4)(193-203.).
80. Zhao, R., et al., *Micro-Flow Visualization of Red Blood Cell-Enhanced Platelet Concentration at Sudden Expansion*. Annals of Biomedical Engineering, 2008. **36**(7): p. 1130-1141.
81. S.Shah, Y.L., *Modeling Particle Shape-Dependent Dynamics in Nanomedicine*. Journal of Nanoscience and Nanotechnology, 2011. **11**(2): p. 919-928.
82. J. F. Douglas, H.E.J., Steve Granick, *A simple kinetic model of polymer adsorption and desorption*. Science, 1993. **262**(24): p. 2010-2012.
83. Park, J.J., et al., *Characterization of Non-Equilibrium Nanoparticle Adsorption on a Model Biological Substrate*. Langmuir, 2010. **26**(7): p. 4822-4830.
84. A. Thomas, D.D., J. Tan, V. Muzykantov, Y. Liu, *Characterization of Nanoparticle Transport and Distribution by Microfluidic Channels*. in preparation, 2011.
85. Whitesides, G.M., et al., *Soft lithography in biology and biochemistry* Annual Review of Biomedical Engineering, 2001. **3**(1): p. 335-373.

86. Wischgoll, T., J.S. Choy, and G.S. Kassab, *Extraction of morphometry and branching angles of porcine coronary arterial tree from CT images*. American Journal of Physiology - Heart and Circulatory Physiology, 2009. **297**(5): p. H1949-H1955.
87. Jr., R.A.F., ed. *Nanomedicine*. Volume I: Basic Capabilities. 1999, Landes Bioscience: Georgetown, TX.
88. Kona, S., et al., *Biodegradable nanoparticles mimicking platelet binding as a targeted and controlled drug delivery system*. International Journal of Pharmaceutics, 2012. **423**(2): p. 516-524.
89. Haun, J.B. and D.A. Hammer, *Quantifying Nanoparticle Adhesion Mediated by Specific Molecular Interactions*. Langmuir, 2008. **24**(16): p. 8821-8832.
90. Cozens-Roberts, C., J.A. Quinn, and D.A. Lauffenberger, *Receptor-mediated adhesion phenomena. Model studies with the Radical-Flow Detachment Assay*. Biophysical Journal, 1990. **58**(1): p. 107-125.
91. Yang, K. and Y.-Q. Ma, *Computer simulation of the translocation of nanoparticles with different shapes across a lipid bilayer*. Nat Nano, 2010. **5**(8): p. 579-583.
92. Shaolie S. Hossain, et al., *Mathematical Modeling of Coupled Drug and Drug-Encapsulated Nanoparticle Transport in Patient-Specific Coronary Artery Walls*, in *ICES Report 10-41*. 2010, The University of Texas at Austin: Austin.
93. Margetts, L., I.M. Smith, and J.M. Leng, *PARALLEL 3D FINITE ELEMENT ANALYSIS OF COUPLED PROBLEMS*, in *III European Conference on Computational Mechanics Solids, Structures and Coupled Problems in Engineering*. 2006: Lisbon, Portugal.
94. Veerapaneni, S.K., et al., *A fast algorithm for simulating vesicle flows in three dimensions*. J. Comput. Phys., 2011. **230**(14): p. 5610-5634.

Vita

Jifu Tan was born in China in 1986. He was awarded bachelor degree with honor in civil engineering in Beijing Jiaotong University in 2007. Following that, he spent two years in studying railway engineering in the graduate school. After that, he joined nanofluidic lab to investigate nanoparticle transport and binding behavior using both computational and experimental approaches. By 2012, he finished his M.S. project in Lehigh University. During M.S. study, he has published several papers on journals. The publications are listed below:

- 1) J. Tan, A. Thomas, and Y. Liu, "Influence of Red Blood Cells on Nanoparticle Targeted Delivery in Microcirculation", *Soft Matter*, 2011 Dec 22;8:1934-1946.
- 2) Y. Liu, J. Tan, A. Thomas, *et al.* "The shape of things to come: importance of design in nanotechnology for drug delivery", *Therapeutic Delivery*, 2012;3 (2): 181-194.
- 3) Y. Wan, J. Tan, *et al.* "Velocity effect on aptamer-based circulating tumor cell isolation in microfluidic devices", *J Phys Chem B*, 2011 Dec 1;115(47):13891-6.